1-1-2013

The SLUGGS survey: wide field imaging of the globular cluster system of NGC 4278

C. Usher
Swinburne University of Technology

D. A. Forbes
Swinburne University of Technology

L. R. Spitler
Macalester College

J. P. Brodie
University of California Observatories

Aaron J. Romanowsky
San Jose State University, aaron.romanowsky@sjsu.edu

See next page for additional authors

Recommended Citation

C. Usher, D. A. Forbes, L. R. Spitler, J. P. Brodie, Aaron J. Romanowsky, J. Strader, and K. A. Woodley. "The SLUGGS survey: wide field imaging of the globular cluster system of NGC 4278" *Monthly Notices of the Royal Astronomical Society* (2013): 1172-1190. https://doi.org/10.1093/mnras/stt1637

Monthly Notices of the ROYAL ASTRONOMICAL SOCIETY

MNRAS **436,** 1172–1190 (2013) doi:10.1093/mnras/stt1637
Advance Access publication 2013 September 25

The SLUGGS Survey: wide field imaging of the globular cluster system of NGC 4278

Christopher Usher,[1]★ Duncan A. Forbes,[1] Lee R. Spitler,[2,3] Jean P. Brodie,[4] Aaron J. Romanowsky,[4,5] Jay Strader[6] and Kristin A. Woodley[4]

[1]*Centre for Astrophysics and Supercomputing, Swinburne University of Technology, Hawthorn, VIC 3122, Australia*
[2]*Department of Physics and Astronomy, Macquarie University, North Ryde, NSW 2109, Australia*
[3]*Australian Astronomical Observatory, PO Box 915, North Ryde, NSW 1670, Australia*
[4]*University of California Observatories, 1156 High Street, Santa Cruz, CA 95064, USA*
[5]*Department of Physics and Astronomy, San José State University, One Washington Square, San Jose, CA 95192, USA*
[6]*Department of Physics and Astronomy, Michigan State University, East Lansing, MI 48824, USA*

Accepted 2013 August 29. Received 2013 August 29; in original form 2013 May 26

ABSTRACT

We use multipointing *Hubble Space Telescope* Advanced Camera for Surveys and wide field Subaru Suprime-Cam imaging to study the globular cluster system of the L* elliptical galaxy NGC 4278. We have also obtained a handful of new globular cluster spectra with the Keck Deep Imaging Multi-Object Spectrograph. We determine the globular cluster surface density profile and use it to calculate the total number of globular clusters, finding the system to be slightly more populous than average for galaxies of its luminosity. We find clear evidence for bimodality in the globular cluster colour distribution and for a colour–magnitude relation in the blue subpopulation (a 'blue tilt'). We also find negative radial colour gradients in both colour subpopulations of equal strength which are similar in strength to those reported in other galaxies. The sizes of NGC 4278's globular clusters decrease with redder colours and increase with galactocentric radius. The ratio of the sizes of blue to red globular clusters is independent of galactocentric radius demonstrating that internal effects are responsible for the size difference with colour.

Key words: Globular cluster: general – galaxies: individual: NGC 4278 – galaxies: star clusters: general.

1 INTRODUCTION

Found in galaxies of all shapes and sizes, globular clusters (GCs) are fossils of galaxy formation as they are among the oldest objects in the Universe (ages >10 Gyr, e.g. Forbes et al. 2001; Puzia et al. 2005; Strader et al. 2005). Extensive optical imaging studies (e.g. Kundu & Whitmore 2001; Larsen et al. 2001) have shown that almost all massive galaxies have bimodal GC colour distributions. Although the origin of the colour bimodality has been debated (e.g. Yoon, Yi & Lee 2006), large spectroscopic studies (e.g. Strader, Beasley & Brodie 2007; Beasley et al. 2008; Alves-Brito et al. 2011; Brodie et al. 2012; Usher et al. 2012) have now shown that most galaxies have bimodality metallicity distributions. Typically the metal-rich, red subpopulations show similar spatial, kinematic and stellar population properties to the galaxy stellar bulges while the metal-poor, blue subpopulations have been tentatively connected to the galaxy's halo (Forbes, Ponman & O'Sullivan 2012, and references therein). Due to the low surface brightness of galaxy haloes and since GCs are much brighter than individual stars, investigations of blue GCs are one of the few ways (other methods include planetary nebula and X-ray hot gas) to study haloes beyond the Local Group.

Here, we study the giant elliptical NGC 4278 ($M_K = -23.8$, Cappellari et al. 2011), part of the Coma I group (Gregory & Thompson 1977; Forbes 1996). NGC 4278 is part of the galaxy sample of the SAGES Legacy Unifying Globulars and GalaxieS Survey[1] (SLUGGS; Brodie et al., in preparation), an ongoing chemodynamical study of nearby early-type galaxies and their GC systems. NGC 4278 hosts a weak radio AGN with observed radio lobes (Giroletti, Taylor & Giovannini 2005) that alternates between LINER-like and Seyfert-like nuclear activity (Younes et al. 2010). The galaxy also hosts a massive, warped H I disc (Morganti et al. 2006), an old, α-element enhanced and solar metallicity (Kuntschner et al. 2010) stellar population with no sign of ongoing

★ E-mail: cusher@astro.swin.edu.au

[1] http://sluggs.swin.edu.au

star formation (Shapiro et al. 2010). The intermediate-luminosity elliptical galaxy NGC 4283 ($M_K = -21.8$ Cappellari et al. 2011) is 3.5 arcmin away from NGC 4278, a separation of 16 kpc at our adopted distance to NGC 4278 of 15.6 Mpc ($m - M = 30.97$), the same distance adopted by Cappellari et al. (2011) for their ATLAS^{3D} survey. The distances, which are based on the surface brightness fluctuation (SBF) distances of Tonry et al. (2001), are consistent with both galaxies being at the same distance. At the adopted distance, NGC 4278's effective radius of $R_e = 32$ arcsec (Cappellari et al. 2011) is equivalent to 2.4 kpc.

The GC system of NGC 4278 was first studied by Harris & van den Bergh (1981) using Canada–France–Hawaii Telescope photographic plates. Forbes et al. (1996) and Kundu & Whitmore (2001) used *Hubble Space Telescope* (*HST*) Wide Field Planetary Camera 2 (WFPC2) *VI*-band imaging to study the GC system but did not find clear evidence of bimodality. Brassington et al. (2009) and Fabbiano et al. (2010) used the WFPC2 imaging to study the connection between low-mass X-ray binaries and GCs in NGC 4278. Chies-Santos et al. (2011a,b, 2012) used William Herschel Telescope Long-slit Intermediate Resolution Infrared Spectrograph *K*-band imaging and *HST* Advanced Camera for Surveys (ACS) *gz*-band imaging of NGC 4278 as part of a larger of study of the near-infrared (NIR) colours of GCs. As part of a SLUGGS study of GC kinematics, Pota et al. (2013, hereafter P13) used Keck Deep Imaging Multi-Object Spectrograph (DEIMOS) spectroscopy to measure the radial velocity of 256 GCs in NGC 4278. In addition to finding clear colour bimodality, they found that the red GCs do not rotate while the blue GCs do. As part of a SLUGGS study of GC metallicity distributions, Usher et al. (2012, hereafter U12) used the same spectroscopy to measure metallicities for 150 GCs and found a bimodal metallicity distribution.

This paper adds to the handful of multipointing *HST* imaging studies of GC systems such as those of NGC 4594 (Spitler et al. 2006; Harris et al. 2010), NGC 4365 (Blom, Spitler & Forbes 2012) and NGC 4649 (Strader et al. 2012). The radial range provided by five ACS pointings of NGC 4278 allows us to study how GC colour and size change with radius. We use the same instrument and filters as well as similar exposure times as the ACS Virgo Cluster Survey (Côté et al. 2004), ACS Fornax Cluster Survey (Jordán et al. 2007) and other multipointing ACS studies such as Blom et al. (2012) and Strader et al. (2012), allowing for direct comparisons. Compared to previous multipointing *HST* GC studies of early-type galaxies, NGC 4278 is a significantly less luminous galaxy. NGC 4278 has a *K*-band luminosity of $6.7 \times 10^{10}\,L_\odot$ while NGC 4594, NGC 4365 and NGC 4649 have *K*-band luminosities of 1.9×10^{11}, 2.5×10^{11} and $3.1 \times 10^{11}\,L_\odot$, respectively (Cappellari et al. 2011). Using the galaxy densities in the Tully & Fisher (1988) catalogue, NGC 4278's environment (1.25 Mpc^{-3}) is intermediate to that of NGC 4594 (0.32 Mpc^{-3}) and of NGC 4365 and NGC 4649 (2.93 and 3.49 Mpc^{-3}, respectively.)

In this paper, we use *HST* ACS and Subaru Suprime-Cam wide field imaging to study the properties of a large number of GCs in NGC 4278. We first describe the imaging reduction before explaining the selection of GC candidates (Section 2). We study the spatial distribution of NGC 4278's GCs and determine the size of the GC system (Section 3.1). In this section, we also investigate the contribution of the nearby galaxy NGC 4283 to NGC 4278's GC system. We then study the colour distribution including second-order effects such as the relationships between magnitude and colour and between galactocentric distance and colour (Section 4). We also use the superior angular resolution of ACS to measure GCs sizes, allowing us to study the relations between GC half-light radii and colour, galactocentric distance and magnitude (Section 5). In Section 6, we summarize our results.

2 DATA ACQUISITION AND ANALYSIS

2.1 *HST* ACS imaging

HST ACS wide field camera images in two bands, *F475W* and *F850LP* (hereafter *g* and *z*), for five pointings were downloaded from the Hubble Legacy Archive. Details of the images are given in Table 1 and the footprints of the pointings are shown in Fig. 1. The ACS imaging extends to 4.5 arcmin from the centre of NGC 4278. The filters and exposure times are similar to those of the ACS Virgo Cluster Survey (Côté et al. 2004) and the ACS Fornax Cluster Survey (Jordán et al. 2007) allowing a direct comparison between our results and those of these two large GC studies. Four of these pointings were previously analysed in P13. A custom pipeline was used to measure aperture photometry (Spitler et al. 2006; Strader et al. 2006). The photometry was calibrated to the AB photometric system using the zero-points of Sirianni et al. (2005). The magnitudes were measured using 5 pixel (0.25 arcsec) apertures. For objects in multiple pointings, we averaged the magnitudes measured in each pointing. In both filters, the difference between the magnitudes measured using a 5 pixel aperture and a 10 pixel aperture is dependent on the half-light radius size of the object. Using the sizes calculated below, a quadratic relation was derived between the half-light radius and the aperture difference for each band. This relation was used to correct each of the measured magnitudes from 5 pixel to 10 pixel apertures. The magnitudes were corrected from 10 pixels to infinity using the corrections provided by Sirianni et al. (2005). The uncertainty in the aperture correction was added in quadrature to the photometric error to give the quoted uncertainty for each total magnitude. Finally, the magnitudes were corrected for extinction using the dust maps of Schlegel, Finkbeiner & Davis (1998).

To help distinguish GCs from stars the superior angular resolution of the ACS data was used to measure the sizes of slightly resolved objects. The DAOPHOT package in IRAF was used to generate empirical point spread functions for each band from bright stars in the images. Each pointing and each filter was measured individually using ISHAPE (Larsen 1999) using circular King (1962) profiles with a concentration parameter fixed at $r_t/r_c = 30$. The uncertainty on the measured sizes was provided by ISHAPE. The weighted average of the *g* and *z* sizes from all pointings was taken as the true half-light radius.

Table 1. *HST* ACS observations.

Pointing centre		Exposures		Programme
RA (°)	Dec. (°)	Filter	Time (s)	ID
185.038 292	29.279 528	*F475W*	676	10835
		F850LP	1240	
185.002 458	29.275 750	*F475W*	702	10835
		F850LP	1200	
185.053 667	29.262 000	*F475W*	702	10835
		F850LP	1200	
185.008 542	29.312 139	*F475W*	702	10835
		F850LP	1200	
185.066 708	29.303 611	*F475W*	758	11679
		F850LP	1287	

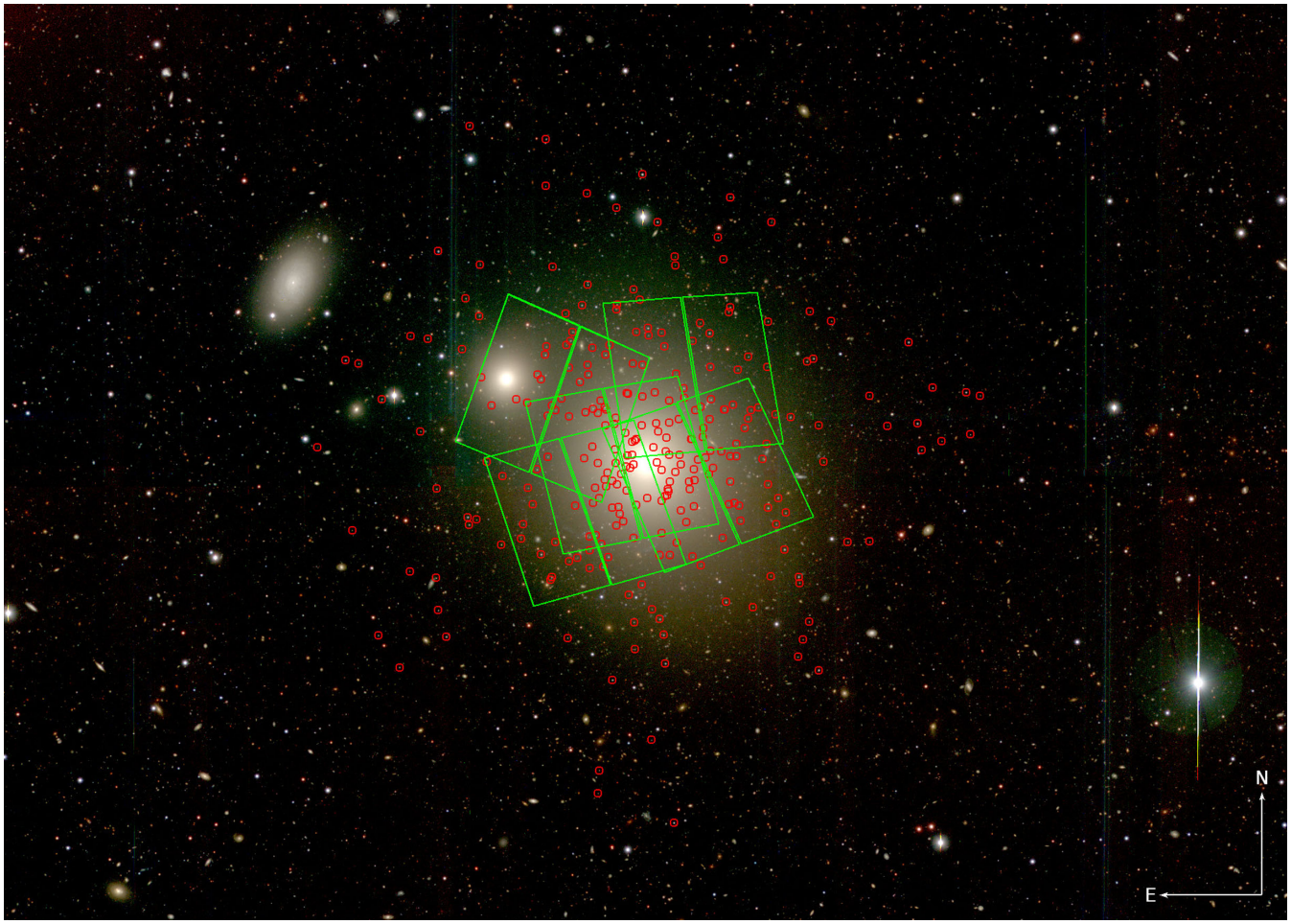

Figure 1. Central 28 × 20 arcmin (125 × 90 kpc) of the Suprime-Cam three filter imaging of NGC 4278. The green lines show the outlines of five ACS pointings. The red circles show the locations of spectroscopically confirmed GCs. The fainter galaxy covered by ACS imaging is NGC 4283; the disc galaxy to the north-east is NGC 4286.

2.2 Subaru Suprime-Cam imaging

To study the GC system out to large galactocentric radii, Subaru Suprime-Cam (Miyazaki et al. 2002) imaging of NGC 4278 was obtained from the Subaru Mitaka Okayama Kiso Archive (Baba et al. 2002) in the *BVI* filters. The Suprime-Cam imaging was observed on 2002 February 13 and covers a field of view of 36 × 29 arcmin centred on NGC 4278. Details of the exposures and the seeing are given in Table 2 and the imaging is shown in Fig. 1.

A modified version of the Suprime-Cam SDFRED package (Yagi et al. 2002; Ouchi et al. 2004) was used to reduce the raw images. Standard aperture photometry techniques using IRAF DAOPHOT package (Stetson 1992) were used to extract the photometric data for point like objects in the images. The astrometry was calibrated to the USNO-B astrometric system (Monet et al. 2003).

Photometry from the Sloan Digital Sky Survey (SDSS) was used to find the photometric zero-points for the Suprime-Cam imaging.

Table 2. Suprime-Cam observations.

Filter	Exposures	Total	Mean seeing
B	3 × 200 s	600 s	1.4 arcsec
V	3 × 150 s	450 s	0.9 arcsec
I	3 × 120 s	360 s	0.9 arcsec

Point-like objects with good Suprime-Cam photometry and GC-like colours more than 1 arcmin from the centre of NGC 4278 were matched with stars in Data Release 7 of the SDSS catalogue (Abazajian et al. 2009). From 280 matching objects with magnitudes $17.6 < i_{\rm SDSS} < 22$, Johnson–Cousins *BVI* magnitudes in the Vega system were calculated using the transformations provided in Ivezić et al. (2007) which are based on the Stetson (2000) extensions of the Landolt (1992) standards to fainter magnitudes. A zero-point including a $(V - I)$ colour term was fitted using weighted least squares to the difference between the instrument magnitudes and the magnitudes calculated from the SDSS photometry. While the colour term is small for the *V* and *I* bands, it is significant for the *B* band. The uncertainties in the zero-point fits were used to estimate the uncertainties in the corrected magnitudes and were added in quadrature to the photometric uncertainties. Finally, the magnitudes were corrected for extinction using the dust maps of Schlegel et al. (1998).

To directly compare the ACS photometry to the Suprime-Cam photometry we used 168 spectroscopically confirmed GCs with both ACS and Suprime-Cam photometry to determine the following relations:

$$(g - z) = (1.72 \pm 0.03) \times (V - I) + (-0.71 \pm 0.03) \quad (1)$$

$$z = I + (-0.25 \pm 0.04) \times (V - I) + (0.62 \pm 0.05). \quad (2)$$

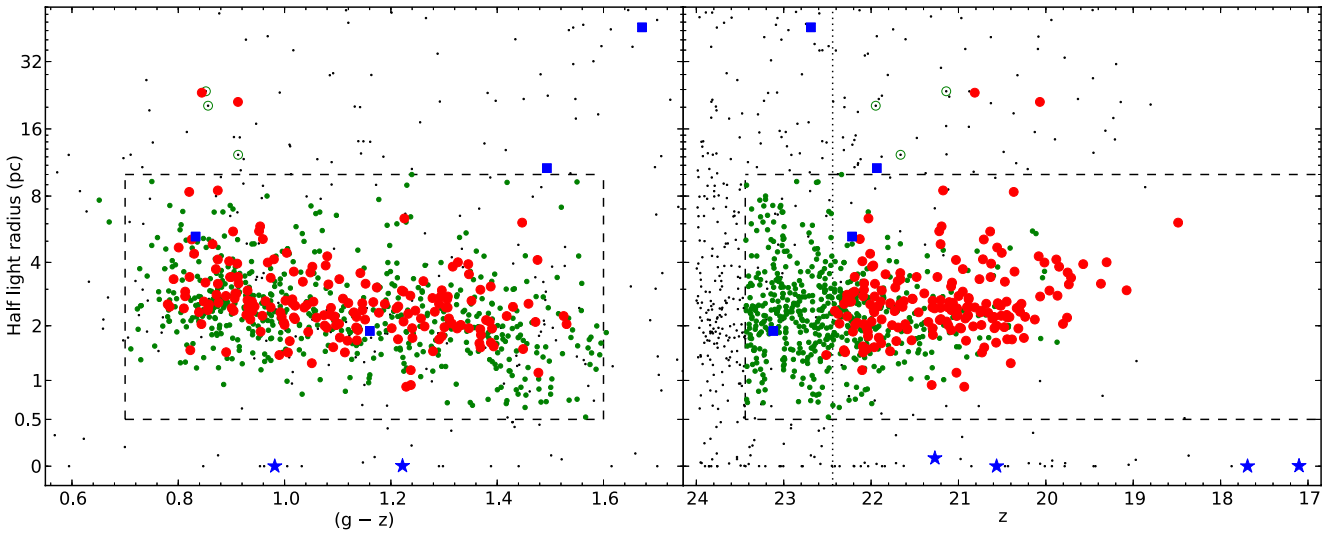

Figure 2. ACS GC selection. Left: half-light radius versus colour selection for the ACS imaging. The small black dots are objects in the ACS imaging brighter than $z = 24$, the small green circles are all objects meeting the selection criteria and the large red circles are spectroscopically confirmed GCs and UCDs. Blue stars are spectroscopically confirmed stars and blue squares are spectroscopically confirmed galaxies. The circled points are UCD candidates. The dashed line box shows the size and colour criteria used to select GC candidates. Right: half-light radius versus magnitude selection for the ACS imaging. The symbols are identical to the left-hand panel and the dashed line box shows the size and magnitude criteria used to select GC candidates. The dotted vertical line is the turnover magnitude of $z = 22.44$. Both panels use an inverse hyperbolic sine scale for the half-light radii. The brightest two stars were observed as guide stars; the remaining two stars were observed to fill the slit masks.

The root-mean-squared difference of both these relations is 0.07 mag and is consistent with the photometric errors.

2.3 GC selection

While the bulk of point-like objects in both the ACS imaging and the Suprime-Cam imaging are GCs, contamination by foreground stars and background galaxies must be removed to produce a clean sample of GC candidates. We used the spectroscopically confirmed GCs to guide our selection of GCs.

GC candidates were selected from objects in the ACS imaging on the basis of their colour, size and magnitude. The colour–size selection is displayed the left-hand side of Fig. 2 and the magnitude–size selection on the right-hand side of Fig. 2. Before this selection was made, objects with irregular morphologies were removed by hand. Objects whose photometric errors put them within the colour range $0.7 < (g - z) < 1.6$ were considered to be candidates. Using the colour–metallicity transformation provided by U12 the limits correspond to [Z/H] $= -2.12$ and [Z/H] $= +0.60$, respectively, while using the colour–metallicity relation of Peng et al. (2006) the limits correspond to [Fe/H] $= -2.61$ and [Fe/H] $= +0.18$. Objects with half-light radii between 0.5 and 10 pc were selected as GC candidates. The lower limit of 0.5 pc includes smaller red GCs while the upper limit was chosen to reject background galaxies. Brodie et al. (2011) adopted 10 pc as the dividing line between GCs and ultracompact dwarfs (UCDs).

Objects were selected as GC candidates if they are brighter than $z = 23.44$. This limit corresponds to one magnitude fainter than the z-band turnover magnitude of the GC luminosity function of $z = 22.44$ which corresponds to the absolute magnitude of $M_z = -8.53$ (Villegas et al. 2010) at the distance of NGC 4278. One magnitude corresponds to the dispersion of the GC luminosity function for a galaxy of NGC 4278 luminosity (Villegas et al. 2010). A colour–magnitude diagram of the ACS GC candidates is shown in Fig. 3. The ACS GC candidates are listed in Table 3, the full version of which appears online.

Objects brighter than the turnover magnitude that are larger than our half-light radius cut of 10 pc but pass the colour cuts were visually inspected. Extended objects with round, regular morphologies are listed in Table 4 as UCD candidates. We do not include these UCD candidates in further analysis.

GC candidates were selected from objects in the Suprime-Cam imaging on the basis of their colour and magnitude. First, extended objects such as background galaxies were rejected by using the difference between measured magnitudes of different sized apertures. The selection in $(B - V)$ versus $(V - I)$ space used to select candidates is shown in Fig. 4. A line was fitted through the spectroscopically confirmed GCs:

$$(B - V) = 1.09 \times (V - I) - 0.28. \quad (3)$$

Objects whose uncertainties put them within three times the scatter (0.05 mag) of the line, within $1.43 < (B - I) < 2.53$ and within $0.82 < (V - I) < 1.34$ were selected. The $(B - I)$ and $(V - I)$ limits correspond to $0.70 < (g - z) < 1.60$. Objects passing the colour cuts were considered GC candidates if their magnitudes were in the range $18.5 < I < 22.5$. The upper magnitude limit was chosen to match the brightest GC candidate in the ACS imaging. A colour–magnitude diagram of the Suprime-Cam GC candidates is shown in Fig. 5. The Suprime-Cam GC candidates are listed in Table 5, the full version of which appears online.

2.4 Keck DEIMOS spectroscopy

In addition to the four Keck DEIMOS slitmasks observed for ∼2 h each in 2010 February and presented in P13, we observed an additional, shallower slitmask on 2013 January 12 with three 600 s exposures. Both the 2010 and 2013 observations used an identical instrument setup of 1 arcsec slits, the 1200 mm^{-1} grating and a

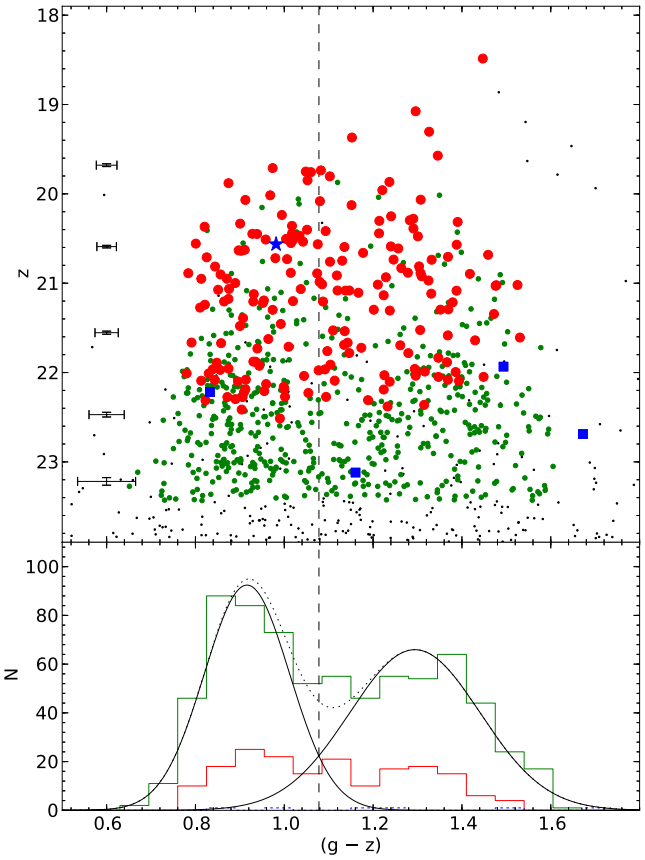

Figure 3. ACS GC candidates. Top panel: ACS colour–magnitude diagram. Black points are objects in the ACS catalogue; green small circles are GC candidates selected by size, colour and magnitude; red circles are spectroscopically confirmed GCs; blue stars indicate spectroscopically confirmed stars; blue squares indicate spectroscopically confirmed galaxies. Mean error bars are shown on the left. Bottom panel: ACS colour histograms. The green histogram is all GC candidates; the red histogram is spectroscopically confirmed GCs; the dashed blue histogram is spectroscopically confirmed stars and galaxies. Overplotted in black are the Gaussian fits from GMM. The black dashed line shows the colour cut $(g - z) = 1.08$ used to divide the sample into red and blue subpopulations.

central wavelength of 7800 Å. Both years' observations were reduced using the DEEP2 SPEC2D pipeline (Cooper et al. 2012; Newman et al. 2013). Radial velocities were measured in an identical manner to P13 by using the IRAF task FXCOR to cross-correlate the observed spectra with 13 template stars observed with DEIMOS. The uncertainty in the radial velocity was estimated in the same way as in P13 by adding in quadrature the uncertainty provided by FXCOR with the standard deviation of the different templates.

We also measured the metallicities of the new GC spectra from the strength of the calcium triplet (CaT) spectral feature using the technique of U12. Single stellar population models show the strength of the CaT is sensitive to metallicity while being insensitive to ages older than 3 Gyr, α-element enhancement and horizontal branch morphology (Vazdekis et al. 2003; Brodie et al. 2012). To reduce the effects of the strong sky line residuals found in the CaT spectral region, we used the method of Foster et al. (2010) of masking the sky line regions and fitting a linear combination of the stellar templates to the observed spectra. We then normalized the fitted spectra and measured the strength of the CaT lines on the normalized spectra. A Monte Carlo resampling technique was used to estimate 68 per cent confidence intervals. To derive a relation between CaT strength and metallicity, U12 measured the strength of the CaT on Vazdekis et al. (2003) model spectra using the same technique as for the observed spectra; we use the same relation (their equation 8). Further details of the metallicity measurement process can be found in U12.

In the case of GCs observed on multiple masks, the radial velocities and metallicities are consistent within observational uncertainties. The simple means of repeated measurements are used in further analysis. Combining the 2013 observations with those presented in P13, we now have 270 (previously 256) confirmed GCs with radial velocities and 155 (previously 150) with spectroscopic metallicity measurements. We plot the CaT metallicities against colour in Fig. 6.

2.5 Comparison with previous work

In their study of GCs using NIR photometry, Chies-Santos et al. (2011a) analysed two of the same ACS pointings as in this work. We found an insignificant mean $(g - z)$ colour difference of 0.003 ± 0.008 and a mean half-light radius ratio of 0.95 ± 0.04 between Chies-Santos et al. (2011a) and our own results. However, we notice a significant difference in the magnitudes with those of Chies-Santos et al. (2011a) being 0.087 ± 0.008 mag fainter in the

Table 3. ACS GC candidates.

Name	RA	Dec.	$(g-z)$	z	r_{hl}	v	[Z/H]	P13	Suprime Cam	Note
	(°)	(°)	(mag)	(mag)	(pc)	(km s^{-1})	(dex)			
(1)	(2)	(3)	(4)	(5)	(6)	(7)	(8)	(9)	(10)	(11)
acs_1369	185.015 995	29.277 228	1.45 ± 0.02	18.49 ± 0.02	6.1 ± 0.3	546 ± 5	$-0.51^{+0.26}_{-0.12}$	NGC 4278_GC261	–	–
acs_1102	185.033 001	29.288 592	1.30 ± 0.01	19.08 ± 0.01	3.0 ± 0.2	479 ± 9	$-0.32^{+0.22}_{-0.23}$	NGC 4278_GC22	–	–
acs_0324	185.023 757	29.280 609	1.33 ± 0.02	19.30 ± 0.01	4.0 ± 0.1	614 ± 6	$-0.72^{+0.22}_{-0.22}$	NGC 4278_GC96	sub_32436	–
acs_1138	185.036 859	29.291 440	1.15 ± 0.01	19.37 ± 0.01	3.2 ± 0.2	886 ± 4	$-0.41^{+0.16}_{-0.17}$	NGC 4278_GC78	sub_33742	–
acs_1115	185.027 438	29.329 398	1.35 ± 0.02	19.57 ± 0.01	3.9 ± 0.1	556 ± 5	$-0.44^{+0.15}_{-0.13}$	NGC 4278_GC65	sub_36928	–
...	...	...	...	...	...	...	...	...	...	...

Notes. Column (1): GC IDs. Column (2) and (3): right ascension and declination in the J2000.0 epoch, respectively. Column (4): $(g - z)$ colour. Column (5): z-band magnitude. Column (6): half-light radius in parsecs. Column (7): radial velocity. Column (8): calcium triplet metallicity. Column (9): identifier from P13. For objects that were observed spectroscopically for the first time in this work, we have extended the P13 naming scheme to them. Column (10): Suprime-Cam identifier if Suprime-Cam candidate. Column (11): Note – G = spectroscopic background galaxy. The full version of this table is provided in a machine readable form in the online Supporting Information.

Table 4. ACS UCD candidates.

Name	RA	Dec.	$(g-z)$	z	$r_{\rm hl}$	v	[Z/H]	Suprime	Note
	(°)	(°)	(mag)	(mag)	(pc)	(km s^{-1})	(dex)	Cam	
(1)	(2)	(3)	(4)	(5)	(6)	(7)	(8)	(9)	(10)
acs_0259	185.004 411	29.293 119	0.91 ± 0.05	20.07 ± 0.03	21.1 ± 0.6	674 ± 14	$-0.79^{+0.29}_{-0.46}$	sub_33897	–
acs_0320	185.046 099	29.242 682	0.84 ± 0.05	20.81 ± 0.04	23.2 ± 0.5	719 ± 18	–	sub_28313	–
acs_1643	185.012 480	29.299 562	0.85 ± 0.05	21.14 ± 0.03	23.6 ± 0.6	–	–	sub_34690	–
acs_1280	185.030 887	29.251 737	0.91 ± 0.05	21.66 ± 0.03	12.3 ± 0.8	–	–	sub_29090	–
acs_0284	184.990 593	29.264 914	1.49 ± 0.08	21.93 ± 0.04	10.7 ± 1.3	$z = 0.35$	–	sub_30229	G
acs_0079	185.005 262	29.320 994	0.86 ± 0.06	21.94 ± 0.04	20.3 ± 1.1	–	–	sub_36325	–

Notes. Column (1): UCD IDs. Column (2) and (3): right ascension and declination in the J2000.0 epoch, respectively. Column (4): $(g - z)$ colour. Column (5): z-band magnitude. Column (6): half-light radius in parsecs. Column (7): radial velocity. Column (8): calcium triplet metallicity. Column (9): Suprime-Cam identifier if Suprime-Cam candidate. Column (10): Note – G = spectroscopic background galaxy.

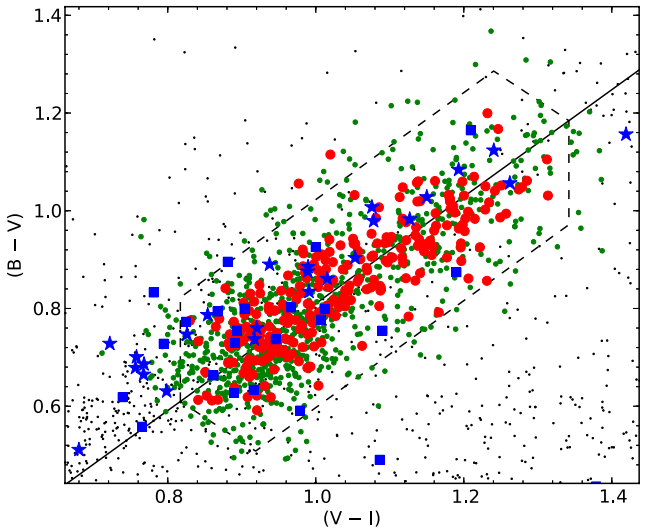

Figure 4. Colour–colour selection for the Suprime-Cam imaging. The small black dots are point-like objects detected in all three Suprime-Cam bands, the small green circles are all objects meeting the selection criteria and the large red circles are spectroscopically confirmed GCs. Blue stars are spectroscopically confirmed stars and blue squares are spectroscopically confirmed galaxies. The solid line shows the $(B - V)$ to $(V - I)$ relation fit to spectroscopically confirmed GCs while the dashed lines are the colour cuts applied. The two spectroscopically confirmed GCs which fail the Suprime-Cam selection criteria have poor Suprime-Cam photometry due to crowding or image artefacts. Both objects are covered by ACS imaging and satisfy the ACS selection criteria.

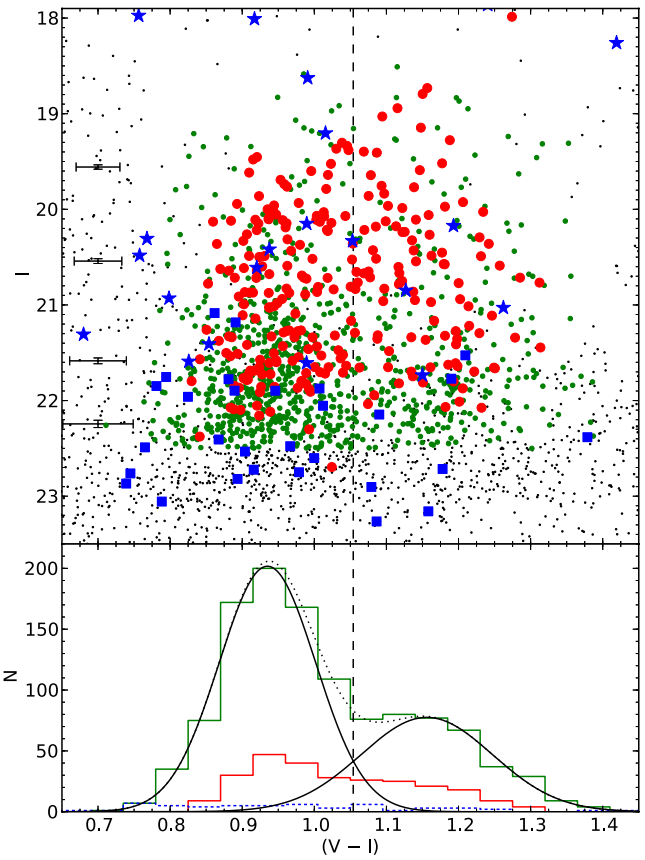

Figure 5. Suprime-Cam GC candidates. Top panel: Suprime-Cam colour–magnitude diagram. Black points are all objects in the Suprime-Cam catalogue; green small circles are GC candidates selected by colour and magnitude; red circles are spectroscopically confirmed GCs; blue stars indicate spectroscopically confirmed stars; blue squares show spectroscopically confirmed galaxies. Mean error bars are shown on the left. Bottom panel: Suprime-Cam colour histograms. The green histogram is GC candidates; the red histogram is spectroscopically confirmed GCs; the dashed blue histogram is spectroscopically confirmed stars and galaxies. Overplotted in black are the Gaussian fits from GMM. The black dashed line shows the colour cut $(V - I) = 1.05$ used to divide the sample into red and blue subpopulations.

g band and 0.084 ± 0.005 in the z band. To investigate this difference, we used the IRAF task QPHOT to measure the magnitudes of ACS GC candidates with 10 pixel apertures and used the same zero-points and the same aperture corrections from 10 pixels to infinity as Chies-Santos et al. (2011a). The mean difference between these QPHOT magnitudes and the magnitudes used in this paper is less than 0.02 mag. The extinction corrections used by Chies-Santos et al. (2011a) differ from ours by only 0.002 mag. Thus, we cannot account for the magnitude difference between Chies-Santos et al. (2011a) and our work. Of the 67 GCs in the Chies-Santos et al. (2011a) catalogue, we identified 66 as GC candidates. The remaining object, GC 59 in Chies-Santos et al. (2011a), appears to be the nucleus of a background galaxy in the ACS imaging.

In their study of the kinematics of the GCs, P13 used four of the five ACS pointings we used in this work and the same Suprime-Cam imaging. The main difference in their analysis of the ACS data was the use of fixed aperture corrections rather than the size-dependent aperture corrections used here. For GC candidates brighter than the turnover magnitude, we find the P13 colours to be on average $(g - z) = 0.010 \pm 0.001$ bluer and their magnitudes to be $z = 0.017 \pm 0.002$ brighter than ours. They used an empirical

Table 5. Suprime-Cam GC candidates.

Name	RA	Dec.	$(B-V)$	$(V-I)$	I	v	[Z/H]	P13	ACS	Note
	(°)	(°)	(mag)	(mag)	(mag)	(km s^{-1})	(dex)			
(1)	(2)	(3)	(4)	(5)	(6)	(7)	(8)	(9)	(10)	(11)
sub_36926	185.264 908	29.329 283	0.94 ± 0.04	1.11 ± 0.03	18.51 ± 0.02	–	–	–	–	–
sub_48443	184.858 638	29.469 100	0.86 ± 0.01	0.99 ± 0.03	18.58 ± 0.02	–	–	–	–	–
sub_33949	184.963 413	29.293 525	0.83 ± 0.01	0.99 ± 0.03	18.63 ± 0.02	-5 ± 6	–	NGC 4278_stars23	–	S
sub_41218	185.029 808	29.385 256	0.91 ± 0.04	1.16 ± 0.03	18.73 ± 0.02	480 ± 6	$-0.72^{+0.16}_{-0.12}$	NGC 4278_GC254	–	–
sub_36266	185.252 633	29.320 075	0.79 ± 0.03	0.95 ± 0.03	18.83 ± 0.02	–	–	–	–	–
...	...	...	...	...	...	...	...	...	...	...

Notes. Column (1): GC IDs. Column (2) and (3): right ascension and declination in the J2000.0 epoch, respectively. Column (4): $(B-V)$ colour. Column (5): $(V-I)$ colour. Column (6): I-band magnitude. Column (7): radial velocity. Column (8): calcium triplet metallicity. Column (9): identifier from P13. For objects that were observed spectroscopically for the first time in this work, we have extended the P13 naming scheme to them. Column (10): ACS identifier if ACS candidate. Column (10): Note – G = spectroscopic background galaxy, S = spectroscopic foreground star. The full version of this table is provided in a machine readable form in the online Supporting Information.

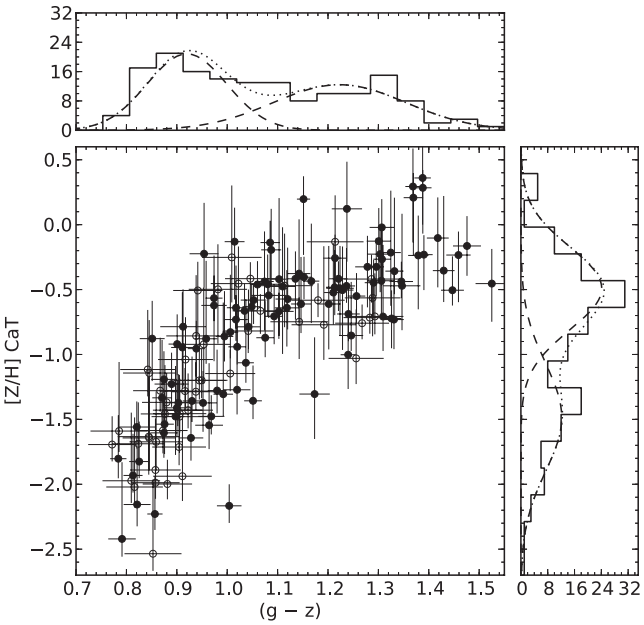

Figure 6. GC colour versus metallicity. On the vertical axis is the CaT-based metallicity; on the horizontal axis $(g-z)$ colour. Solid points have ACS photometry while open points are GCs with Suprime-Cam $(V-I)$ colours transformed into $(g-z)$. The plot to the right is the metallicity histogram; the plot on top is the colour histogram. The bimodal GMM fits are plotted over the histograms. Both the colour and metallicity distributions are bimodal. The relationship between colour and metallicity is non-linear.

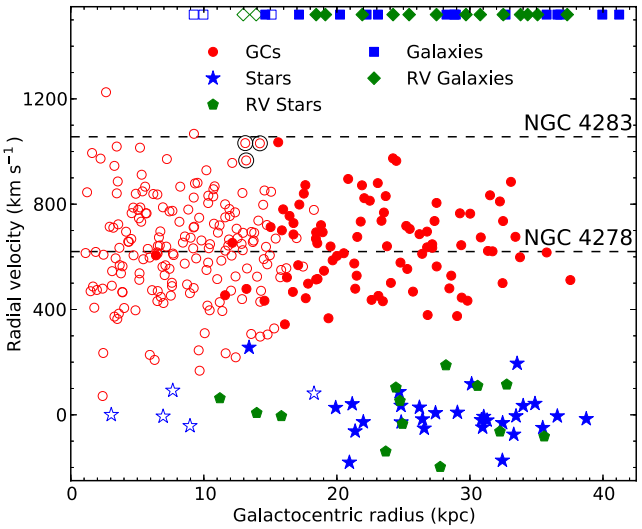

Figure 7. Selection of spectroscopic GCs. Red circles are spectroscopically confirmed GCs. Blue stars are spectroscopically confirmed stars that do not meet the criteria to be GC candidates. Although the star sub_27283 ($v = 256 \pm 12$ km s^{-1}) has a GC like radial velocity, it has a non-zero proper motion in the USNO-B catalogue (Monet et al. 2003). Green pentagons are spectroscopically confirmed stars that meet the GC candidate criteria. Blue squares are spectroscopically confirmed background galaxies that do not the meet the criteria for GC candidates. Green diamonds are spectroscopically confirmed galaxies that meet GC candidate selection criteria. Hollow points have ACS coverage; solid points have only Suprime-Cam coverage. For objects in both imaging data sets, we have preferred the ACS selection. The background galaxies have been given an artificial radial velocity of 1520 km s^{-1}; in reality, their redshifts are significantly higher. The black dashed lines are the systemic velocities of NGC 4278 and NGC 4283. The three circled GCs can be identified with NGC 4283.

transformation to convert the colours of objects with only Suprime-Cam photometry into $(g-z)$.

We can compare the spectroscopic classification of objects with our imaging-based selection. We plot the location of the spectroscopic objects in phase space in Fig. 7 and list them in Appendix A. Two of the ACS GC candidates, acs_2494 and acs_2464, and one of the UCD candidates, acs_0284, appear to be background galaxies based on the presence of significantly redshifted emission lines while 13 of the Suprime-Cam candidates also appear to be background galaxies due to redshifted emission lines in their spectra. Unfortunately, NGC 4278's low systemic velocity ($v_{\rm sys} = 620$ km s^{-1}; Cappellari et al. 2011) makes separating foreground stars from GC on the basis of their radial velocities more difficult. Guided by ACS size measurements, P13 used a friendless algorithm to determine which objects are stars. Two of the objects (sub_29204 and sub_35980) observed in 2013 January have low enough radial velocities (27 ± 5 and -181 ± 27 km s^{-1}, respectively) to unambiguously make them stars. However, a third object (sub_27283) observed in 2013 January is more problematic as its radial velocity (256 ± 12) overlaps with that of GCs at the same galactocentric radius. It fails the Suprime-Cam GC selection criteria and is bluer ($V-I = 0.75$) than any of the spectroscopically confirmed GCs. In the USNO-B astrometry catalogue, sub_27283 has a non-zero proper motion indicating that it is a foreground star. Although some of the stars at larger radii have radial velocities of about 200 km s^{-1} and could belong to the low-velocity tail of the GC distribution, these stars are

well separated from the GCs at the same radius in velocity. None of the ACS GC candidates but 13 of the Suprime-Cam candidates have radial velocities consistent with being stars. In our subsequent analysis, we did not remove GC candidates known spectroscopically to be stars or galaxies from our analysis nor did we remove Suprime-Cam candidates that failed the ACS candidate criteria. For the ACS data set removing, the two spectroscopically identified galaxies has no effect on our results. If we removed spectroscopic and ACS contaminants from the Suprime-Cam data set, the surface density of contaminants would be much lower in the inner regions than in the outer regions. When we use the Suprime-Cam data, we address the effects of contaminants on our results.

3 GC SPATIAL DISTRIBUTION AND SYSTEM SIZE

The relative number of a GCs in a galaxy is usually expressed by the specific frequency, which is the number of GCs normalized by the V-band luminosity (Harris & van den Bergh 1981). The most and least massive galaxies have higher specific frequencies on average than intermediate mass galaxies (Forbes 2005; Peng et al. 2008). Intriguingly, both the total galaxy halo mass (Spitler & Forbes 2009; Georgiev et al. 2010) and the mass of the central supermassive black hole (Burkert & Tremaine 2010; Harris & Harris 2011; Rhode 2012) scale nearly linearly with the total number of GCs in a galaxy. Thus, the total number of GCs can be used to estimate two important galaxy properties that are difficult to directly measure. As stellar mass, halo mass and black hole mass are all correlated, it is unclear which is the fundamental relation.

In addition to their use in estimating the size of GC populations, GC surface density profiles are an important ingredient in using GC kinematics in mass modelling. In almost all galaxies, the blue GC subpopulation is more spatially extended than the red subpopulation (e.g. Faifer et al. 2011; Hargis & Rhode 2012; P13). The radial surface density profile of the red subpopulation usually closely follows the bulge surface brightness profile while the blue surface density profile seems to be closer to the X-ray gas surface brightness profile, suggesting that it traces the galaxy's halo (Forbes et al. 2012).

3.1 Spatial distribution

To study the radial distribution of GCs in NGC 4278 we used GC candidates brighter than the turnover magnitude to produce surface density profiles for the total GC system as well as for each of the subpopulations. A z-band turnover magnitude of $z = 22.44$ was used for the ACS candidates while a I-band turnover of $I = 22.12$, equivalent to the z-band turnover for a GC with $(V - I) = 1.05$, was used for the Suprime-Cam candidates. We used the colour splits of $(g - z) = 1.078$ and $(V - I) = 1.054$ (derived in Section 4) to divide the total system into red and blue subpopulations. No attempt was made to correct for magnitude incompleteness or contamination. Candidates were sorted by galactocentric radius and placed into bins of equal size. The area and mean radius were calculated for each bin accounting for the incomplete azimuthal coverage of the ACS imaging at larger radii. For the radial range with both ACS and Subprime-cam candidates, we see good agreement between the two data sets, despite the different selection criteria and quality of the data sets. The surface density profiles were fitted with Sérsic (1963) profiles with constant, free background terms. The following

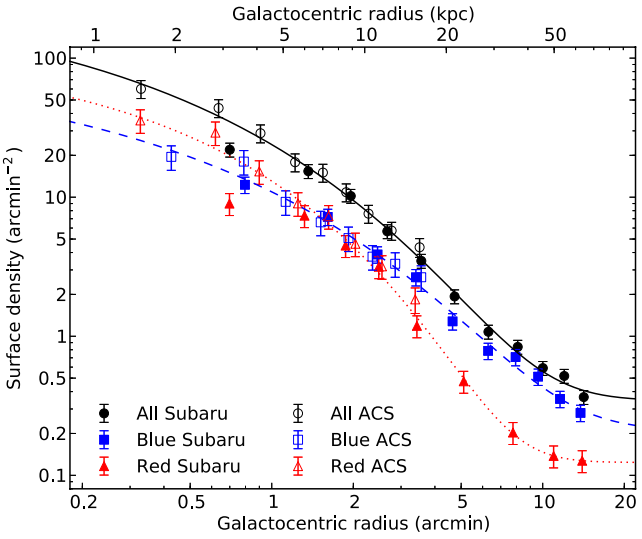

Figure 8. Surface density profiles for the red (dotted line, triangles) and blue (dashed line, squares) GC subpopulations as well as the total population in black (solid line, circles). ACS data are open symbols; Suprime-Cam data are solid symbols. The innermost Suprime-Cam points are likely affected by incompleteness and are not included in the fits. In the range of overlap between the ACS and Suprime-Cam data we see good agreement. The solid lines are Sérsic fits including a constant background. The red subpopulation is more centrally concentrated than the blue subpopulation. The red subpopulation reaches a background level of about 0.11 objects per square arcmin at about 14 arcmin.

variation of equation 1 from Graham & Driver (2005) was fitted:

$$N(R) = N_{\rm e} \exp\left(-b_n\left[\left(\frac{R}{R_{\rm e}}\right)^{1/n} - 1\right]\right) + bg, \quad (4)$$

where $b_n = 1.9992n - 0.3271$. The free parameters of the fit are the surface density $N_{\rm e}$ at the effective radius, the effective radius $R_{\rm e}$, the Sérsic index n and the constant background bg. The innermost Suprime-Cam point for each subpopulation was not included in the fits due to the probable incompleteness. The measured surface densities and the fitted profiles are shown in Fig. 8 while the results of the fits are provided in Table 6. The uncertainties in the fitted parameters were estimated using bootstrapping; we note that there are significant correlations between the fitted parameters especially for the blue subpopulation. As shown in Fig. 13, the background surface density is consistent with the number of spectroscopically observed contaminants.

As in other galaxies, the red subpopulation is more centrally concentrated than the blue subpopulation. The red subpopulation

Table 6. GC surface density fits.

Sample (1)	$N_{\rm e}$ (2)	$R_{\rm e}$ (3)	n (4)	bg (5)	Total (6)
All	$5.1^{+2.0}_{-0.5}$	$2.8^{+0.1}_{-0.5}$	$2.2^{+0.2}_{-0.5}$	$0.35^{+0.11}_{-0.02}$	1378^{+29}_{-195}
Blue	$1.5^{+0.8}_{-0.6}$	$4.3^{+1.6}_{-1.0}$	$2.3^{+0.8}_{-0.6}$	$0.21^{+0.07}_{-0.08}$	930^{+237}_{-188}
Red	$5.4^{+0.8}_{-1.0}$	$1.8^{+0.1}_{-0.1}$	$1.7^{+0.3}_{-0.3}$	$0.12^{+0.02}_{-0.02}$	509^{+25}_{-41}

Notes. Column (1): GC subpopulation. Column (2): GC surface density at the effective radius in arcmin^{-2}. Column (3): effective radius in arcmin. Column (4): Sérsic index. Column (5): background surface density in arcmin^{-2}. Column (6): total number of GC in each subpopulation.

reaches a background at a radius of about 14 arcmin while the blue subpopulation does not seem to have reached a background within the Suprime-Cam field of view. We can check the background surface densities in two ways. In Section 4.2, we find that the number of Suprime-Cam candidates that are shown to be contaminants spectroscopically is consistent with the background surface densities. 14 Subaru candidates fail the ACS selection criteria – 6 are likely stars and the remainder galaxies. Using the area of the ACS observations these contaminants correspond to surface densities of 0.379 ± 0.101, 0.271 ± 0.086 and 0.108 ± 0.054 arcmin^{-2} for all, blue and red, respectively, which are consistent with the fitted values. We integrated the Sérsic profiles to determine the total numbers of GCs and doubled the total to account for only having measured the surface density of GCs brighter than the turnover magnitude. We estimate 1378^{+32}_{-194} GCs in total, 930^{+315}_{-176} blue GCs and 509^{+27}_{-40} red GCs. The total, blue and red fits have χ^2 values of 7.7 (15 degrees of freedom), 8.0 (13 degrees of freedom) and 6.9 (12 degrees of freedom), respectively, indicating that they are good fits. Assuming a V-band absolute magnitude of $M_V = -20.9 \pm 0.2$ (de Vaucouleurs et al. 1991), we find a specific frequency of $6.0^{+1.2}_{-1.3}$ for NGC 4278.

In addition to the radial distribution of GCs, we examined their azimuthal distribution. In the radial region with complete ACS azimuthal coverage (galactocentric radius less than 2.5 arcmin), Kolmogorov–Smirnov (KS) tests revealed that the azimuthal distributions of all ACS candidates brighter than the turnover magnitude were consistent with being drawn from a uniform distribution (p-value of 0.76). When split by colour the blue and red candidates are also each consistent with being drawn from uniform azimuthal distributions (p-values of 0.45 and 0.23, respectively). Since the GC distribution is consistent with being circular, the circular galactocentric radii used throughout this work are valid. NGC 4278 is a rather round galaxy (K-band axis ratio = 0.91; Skrutskie et al. 2006) and is like other galaxies in having similar ellipticities for its GC and field star populations (Brodie & Strader 2006; Park & Lee 2013).

Remarkably, using object counts on photographic plates, Harris & van den Bergh (1981) estimated a GC system size of 1075 ± 125, in agreement with our value of 1378^{+32}_{-194}. For its absolute magnitude, NGC 4278 has a relatively high specific frequency of $6.0^{+1.2}_{-1.3}$ compared to galaxies of similar luminosity in the large ACS study of Peng et al. (2008). We note that Blom et al. (2012) found large differences in S_N between *HST*-based studies with small radial extent such as Peng et al. (2008) and those using wide field imaging. Compared to the heterogeneous catalogue of specific frequencies of Harris, Harris & Alessi (2013), NGC 4278's specific frequency is higher than most other galaxies of similar luminosity but within the scatter. Using a mean GC mass of $4 \times 10^5\,M_\odot$ and the ratio of halo mass to GC system mass from Spitler & Forbes (2009), we estimate that NGC 4278 has a total halo mass of $8 \times 10^{12}\,M_\odot$. Using equation 8 of Rhode (2012), we predict a central black hole mass of $(3.8 \pm 0.5) \times 10^8\,M_\odot$ for NGC 4278 based on the number of GCs.

The uncertainty in the specific frequency is affected by the uncertainty of the distance. The distance has two effects on the specific frequency. First, it changes the GC turnover magnitude. If too faint a turnover magnitude is used, the number of GC will be overestimated while a too bright turnover magnitude would cause the number of GCs to be underestimated. Secondly, the distance effects absolute magnitude. A higher absolute magnitude reduces the specific frequency. Since both these act in the same direction their effects partially cancel each other out. A distance modulus 0.2 mag too low would result in an overestimation of the GC population by 19 per cent and an underestimation of the luminosity by 17 per cent, resulting in a specific frequency only 1 per cent too high. Beyond the distance-based uncertainty, Villegas et al. (2010) showed that there is cosmic scatter in the GC turnover magnitude at a level of 0.2 mag; they found that the mean absolute turnover magnitudes of the Virgo and Fornax clusters disagree by 0.2 mag.

3.2 The distance to NGC 4278

In this work, we adopted a distance modulus of $(m - M) = 30.97$ (15.6 Mpc) which is based on the Tonry et al. (2001) SBF distance of $(m - M) = 31.03 \pm 0.20$ shifted by 0.06 to match the mean of the *HST*-based SBF distances in the Virgo Cluster from Mei et al. (2007). The distance to NGC 4278 has also been estimated by using the GC luminosity function by Forbes (1996) and Kundu & Whitmore (2001) who found distance moduli of 30.61 ± 0.14 and 31.11 ± 0.11. While the Kundu & Whitmore (2001) value is consistent with the SBF distance, the Forbes (1996) distance is significantly lower. We note that the Forbes (1996) GC luminosity function distance to NGC 4494 is similarly lower than the SBF distance from Tonry et al. (2001). As noted before, Villegas et al. (2010) showed that there seems to be significant scatter caused by using the GC luminosity function as a distance indicator. Additionally, Jacoby, Ciardullo & Harris (1996) used the planetary nebula (PN) luminosity function to measure the distance to NGC 4278 as 30.04 ± 0.16. However, their luminosity function was based on only 23 PN candidates and they noted that NGC 4278 has an unusual PN luminosity function with an overabundance of bright PN candidates. Furthermore, it is known that using PN luminosity functions give systematically lower distances than SBF distances (Ciardullo et al. 2002; Ciardullo 2012). Although they are less precise, distances based on the Fundamental Plane are consistent with our adopted distance (Blakeslee et al. 2001; Cappellari et al. 2013).

With our data set we can test our adopted distance through two independent techniques. First, by assuming that the mean size of GCs is the same in galaxies of similar mass (an assumption supported by observations e.g. Masters et al. 2010; see Section 5), we can use the mean angular size of the GCs (0.0349 ± 0.0007 arcsec) as a geometric distance estimator. Using the mean GC size in the Virgo and Fornax galaxies of similar luminosity to NGC 4278 from Masters et al. (2010), we get a distance to NGC 4278 of 16.0 ± 1.0 Mpc while using the mean GC size in the Milky Way (free of any uncertainty in the extragalactic distance scale) from Jordán et al. (2005) gives a distance of 15.0 ± 0.7 Mpc. Both of these are in perfect agreement with our adopted distance. Secondly, we can use the GC luminosity function to constrain the distance. In Fig. 9, we plot the observed g- and z-band luminosity functions along with the luminosity functions predicted from our adopted distance and the turnover magnitudes and magnitude dispersions from Villegas et al. (2010). The observed luminosity functions appear to be consistent with the predicted luminosity functions. Although due to incompleteness the observed turnover magnitude could be brighter than its true value, the observations do not support as bright a turnover magnitude as would be required for the PN luminosity function distance or the Forbes (1996) GC luminosity function distance. On the basis of GC sizes and the GC luminosity function, we can conclude that our adopted SBF-based distance is reasonable. We note that only two of our results are based on the distance to NGC 4278: the absolute size of the GCs and the total number of GCs.

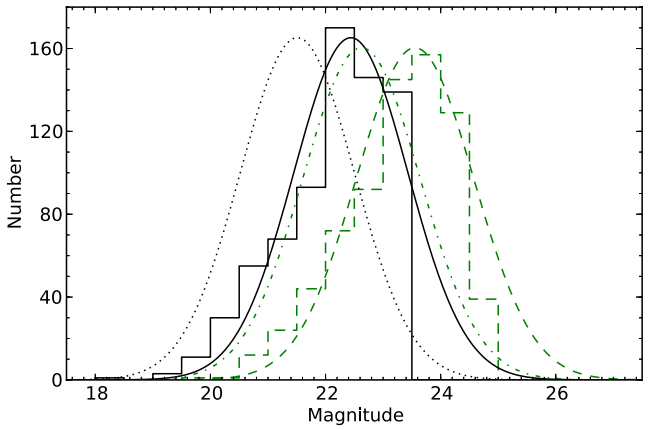

Figure 9. GC luminosity functions. The green dashed-line histogram is the observed g-band magnitude histogram; the black solid-line histogram is the z-band magnitude histogram. Note that GC candidates are limited to be brighter than $z = 23.44$. The green dashed-line and black solid line curves are the Gaussian luminosity functions for the g- and z-bands, respectively, based on the turnover magnitudes ($\mu_g = -7.41$, $\mu_z = -8.53$) and dispersions ($\sigma_g = 1.02$, $\sigma_z = 0.99$) from Villegas et al. (2010) for a galaxy of NGC 4278's absolute magnitude and our adopted distance modulus of ($m - M = 30.97$). Our adopted distance seems to be consistent with observed GC luminosity functions. The green dot–dashed line and black dotted line curves are the Gaussian luminosity functions for the g- and z-bands, respectively, using the same absolute turnover magnitude and dispersions but the PN luminosity function distance modulus of Jacoby et al. (1996). This distance is inconsistent with the observed GC luminosity function.

3.3 The GC system of NGC 4283

We also investigated the contribution of NGC 4283's GC system to NGC 4278's GC system. NGC 4283 is at a projected distance of 16 kpc in the sky and has a SBF distance consistent with NGC 4278's distance (Tonry et al. 2001). The systemic velocities of the two galaxies (NGC 4278 $v_{\rm sys} = 620$ km s^{-1}, NGC 4283 $v_{\rm sys} = 1056$ km s^{-1}; Cappellari et al. 2011) differ by 436 km s^{-1}. Adopting an absolute magnitude of $M_V = -19.0$ (de Vaucouleurs et al. 1991) and a specific frequency of 1.3, typical of galaxies of this absolute magnitude (see table 3 of Peng et al. 2008), we would expect NGC 4283 to have only 26 GCs brighter than the turnover magnitude.

While we do not see an overdensity of Suprime-Cam GC candidates near NGC 4283, we do see a slight overdensity in ACS GC candidates near NGC 4283. Harris & van den Bergh (1981) also did not find an obvious overdensity of sources around NGC 4283 in their photographic plate. We used the GC surface density profile measured above to estimate how many GCs brighter than the turnover we would expect near NGC 4283 from NGC 4278's GC system. Within 1.5 kpc of NGC 4283 we would only expect 1.1 GCs, although we see five GCs candidates in the same area. In 100 000 realizations of the GC system, we only saw this many GCs within 1.5 kpc of NGC 4283 in 578 realizations. We expect 11.3 GCs within 5 kpc; we see 15 GC candidates within 5 kpc. Making the rough assumption that the half number radius of NGC 4283's GC system is 5 kpc, we can estimate that NGC 4283 has a total of 16 ± 12 GCs.

If NGC 4283 GCs made a significant contribution to NGC 4278's GC system, we would expect NGC 4283 GCs to show up in phase space as interlopers. Unfortunately, the velocity difference between the galaxies is not large enough to cleanly separate the GC populations. Using the velocity rms of NGC 7457 (68 km s^{-1}) from P13, the galaxy closest to NGC 4283 in K-band luminosity in P13, as an upper limit on NGC 4283's GC velocity rms, three GCs – acs_0641 (1031 km s^{-1}), acs_1900 (966 km s^{-1}) and acs_2206 (1032 km s^{-1}) – lie within 5 kpc on the sky and within 136 km s^{-1} of NGC 4283. These three GCs are highlighted in Fig. 7. This suggests that the three GCs may be part of the NGC 4283 GC system. However, due to the small velocity difference between the galaxies we cannot rule out that they are part of the NGC 4278 GC system. Assuming that all three are truly NGC 4283 GCs and that the radial velocity observations sampled both galaxy's populations with equal likelihood, we would only expect NGC 4283 to have $3/267 = 1.1$ per cent as many GCs as NGC 4278. Above we determine that NGC 4278 has 1378 GCs; using this radial velocity argument, we can estimate that NGC 4283 has 15 ± 9 GCs.

The number of NGC 4283 GCs is insignificant compared to the NGC 4278 population. We found no effect on the results of the colour–magnitude (Section 4.1), colour–radius (Section 4.2) or size (Section 5) relations nor on the surface density profiles (Section 3.1) due to NGC 4283. If NGC 4283 has 16 ± 8 GCs, it would have a specific frequency of 0.4 ± 0.2. While this is lower than the mean of 1.3 for galaxies of similar luminosities in Peng et al. (2008), it is within the range of values they found. Likewise it is within the range of specific frequencies observed for galaxies of similar luminosity in the Harris et al. (2013) catalogue.

In the Virgo Cluster, the dwarf galaxies closest to giant galaxies show the lowest specific frequencies of any galaxies in the Peng et al. study. These galaxies are thought to have lost GCs through stripping. If NGC 4283 has interacted with NGC 4278 it could have lost some of its GC population to NGC 4278. To double the specific frequency of NGC 4283 by having it further away than our adopted distance would require it to be twice as distant, a distance strongly disfavoured by the SBF distance.

4 GC COLOURS

As can be seen in Figs 3 and 5, NGC 4278 possesses the GC colour bimodality found in almost all massive galaxies (e.g. Kundu & Whitmore 2001; Larsen et al. 2001). This colour bimodality was previously noted by P13 and U12 who used much the same data as this paper. We used the Gaussian Mixture Modelling (GMM) code of Muratov & Gnedin (2010) to confirm colour bimodality. GMM finds both the best-fitting unimodal and bimodal distributions to the data before using a parametric bootstrap to determine whether or not the bimodal distribution is an improved fit over the unimodal. However, as Muratov & Gnedin (2010) note, GMM is more a test of non-Gaussianity than of bimodality. They suggest using the relative separation of the fitted peaks and the kurtosis of the distribution to help determine whether a distribution is bimodal. We adopted their requirements of relative peak separation of $D = 2$ and a negative kurtosis, in addition to a high probability from GMM, to call a distribution bimodal.

Results of the GMM tests are given in Table 7. We confirm colour bimodality in the GC candidates, spectroscopically confirmed GCs and the GCs with CaT measurements, in line with previous conclusions by P13 and U12. The peak locations, peak widths and the fraction of blue clusters are all in agreement with the previous work. For ACS candidates, we found equal probability of being red or blue at $(g - z) = 1.078$ while for the Suprime-Cam candidates we found equal probability of being in either colour subpopulation at $(V - I) = 1.054$. We used these colour splits to divide the GC candidates into red and blue subpopulations. The fraction of blue and red Suprime-Cam candidates are consistent with numbers of

Table 7. Colour and metallicity distribution bimodality results from GMM.

Sample	Colour (mag)	N	$\mu_{\rm blue}$ (mag)	$\sigma_{\rm blue}$ (mag)	$\mu_{\rm red}$ (mag)	$\sigma_{\rm red}$ (mag)	$f_{\rm blue}$	p	D	k
(1)	(2)	(3)	(4)	(5)	(6)	(7)	(8)	(9)	(10)	(11)
ACS All	$(g-z)$	716	0.916 ± 0.016	0.096 ± 0.010	1.294 ± 0.024	0.147 ± 0.013	0.478 ± 0.049	>0.999	3.05 ± 0.20	−1.11
ACS Turnover	$(g-z)$	410	0.948 ± 0.023	0.102 ± 0.015	1.330 ± 0.031	0.107 ± 0.020	0.558 ± 0.068	>0.999	3.66 ± 0.31	−1.29
ACS RV	$(g-z)$	181	0.912 ± 0.046	0.074 ± 0.028	1.212 ± 0.061	0.150 ± 0.032	0.466 ± 0.160	>0.999	2.54 ± 0.43	−1.07
ACS CaT	$(g-z)$	105	0.997 ± 0.038	0.110 ± 0.020	1.303 ± 0.040	0.096 ± 0.024	0.605 ± 0.132	>0.988	2.96 ± 0.38	−1.04
S-Cam All	$(V-I)$	1146	0.935 ± 0.004	0.067 ± 0.003	1.156 ± 0.010	0.091 ± 0.006	0.657 ± 0.029	0.990	2.76 ± 0.19	−0.36
S-Cam Turnover	$(V-I)$	901	0.937 ± 0.005	0.063 ± 0.003	1.156 ± 0.011	0.090 ± 0.007	0.634 ± 0.034	>0.999	2.82 ± 0.22	−0.46
S-Cam < 30 kpc	$(V-I)$	508	0.943 ± 0.006	0.062 ± 0.004	1.149 ± 0.014	0.082 ± 0.008	0.581 ± 0.040	>0.999	2.84 ± 0.24	−0.67
S-Cam RV	$(V-I)$	257	0.941 ± 0.012	0.048 ± 0.009	1.118 ± 0.024	0.085 ± 0.012	0.495 ± 0.101	>0.999	2.55 ± 0.39	−0.82
S-Cam CaT	$(V-I)$	153	0.924 ± 0.011	0.037 ± 0.008	1.089 ± 0.017	0.088 ± 0.011	0.358 ± 0.091	>0.999	2.45 ± 0.35	−0.84
All CaT	$(g-z)$	155	0.920 ± 0.035	0.079 ± 0.022	1.223 ± 0.059	0.132 ± 0.029	0.501 ± 0.147	>0.999	2.79 ± 0.54	−0.99
All CaT	[Z/H]	155	-1.49 ± 0.14	0.42 ± 0.09	-0.49 ± 0.05	0.32 ± 0.06	0.397 ± 0.101	>0.999	2.68 ± 0.52	−0.45

Notes. Column (1): GC sample. Column (2): colour. Column (3): number of GCs. Column (4): mean colour of the blue subpopulation. Column (5): dispersion of the blue subpopulation. Column (6): mean colour of the red subpopulation. Column (7): dispersion of the red subpopulation. Column (8): fraction of the GCs in the blue subpopulation. Column (9): p-value that a bimodal fit is preferred over a unimodal fit. Column (10): separation of the GMM peaks normalized by their width. Column (11): the kurtosis of the sample. For GCs with CaT measurements but no $(g-z)$ colours, we used equation (1) to convert $(V-I)$ into $(g-z)$.

blue and red GCs calculated from the surface density profiles in Section 3.1. The $(g-z)$ colour peaks and the fraction of blue GCs of NGC 4278 agree with the relations as a function of galaxy B-band absolute magnitude of Strader et al. (2006) and Peng et al. (2006).

Contamination affects the overall colour distributions, masking or mimicking bimodality. The ACS data set has a low level of contamination since the size cut removes foreground stars and extended background galaxies and since the ACS candidates are close to the centre of the galaxy where the surface density of GCs is much higher than that of the contaminants. Therefore, the observed ACS colour distributions likely reflect the true colour distributions. However, the Suprime-Cam data set has a significant level of contamination as both stars and galaxies overlap with GCs in colour–colour space. Additionally the Suprime-Cam data extend to large radii where the surface density of contaminants is comparable to that of GCs. Using the surface density of contaminants from Section 3.1, we can estimate that 39 and 40 per cent, respectively, of the blue and red Suprime-Cam GC candidates that are brighter than turnover are contaminants. We ran GMM on Suprime-Cam candidates brighter than the turnover magnitude within 30 kpc (more than twice the half number radius of the GC system; see Table 6) of the centre of the galaxy. The GMM results of this sample were consistent with those of all Suprime-Cam candidates brighter than turnover despite the contaminant rate being approximately four times lower. This suggests that the general shape of the Suprime-Cam colour distribution is not affected by contamination. The colour distributions of the spectroscopically confirmed GCs is quite similar to those of candidates brighter than turnover for both the ACS and Suprime-Cam data sets (KS probabilities of 0.29 and 0.87, respectively, within the same radial ranges, that the spectroscopically confirmed GCs are drawn from the same distributions as the candidates).

We also ran GMM on the CaT metallicity distribution, finding clear evidence for bimodality. Unsurprisingly, adding only five new CaT measurements does not change the results from U12. Likewise the colours of the GCs with CaT measurements show bimodality. The CaT metallicity and colour distributions along with their GMM fits may be seen in Fig. 6. The relationship between GC colour and metallicity is clearly non-linear in NGC 4278 as has been seen in previous observational studies such as Peng et al. (2006) and U12, and theoretical models such as Conroy, Gunn & White (2009) and Yoon et al. (2011). Due to this non-linear relation, the shape of the colour distribution is different than the shape of the metallicity distribution.

4.1 The blue tilt

First described by Spitler et al. (2006), Strader et al. (2006) and Harris et al. (2006), the blue tilt is a colour–magnitude relation where the brighter GCs in the blue subpopulation are redder than the fainter blue subpopulation GCs. This relation is found in most but not all (i.e. NGC 4472; Spitler et al. 2006) galaxies with sufficient numbers of GCs. No clear colour–magnitude relation has been seen for the red subpopulations. The blue tilt is seen in both high-mass and low-mass galaxies but is weaker in low-mass galaxies (Mieske et al. 2010). The strength of the blue tilt decreases at fainter magnitudes (Harris 2009a). Since colour traces metallicity and magnitude traces mass, the blue tilt is a mass–metallicity relationship. Strader & Smith (2008) and Bailin & Harris (2009) explain the observed mass–metallicity relations as self-enrichment where the more massive GCs are able to hold on to metals from the first generation of GC stars and incorporate the metals into later stellar generation(s). Less massive GCs are not able to hold on to the metals, explaining the

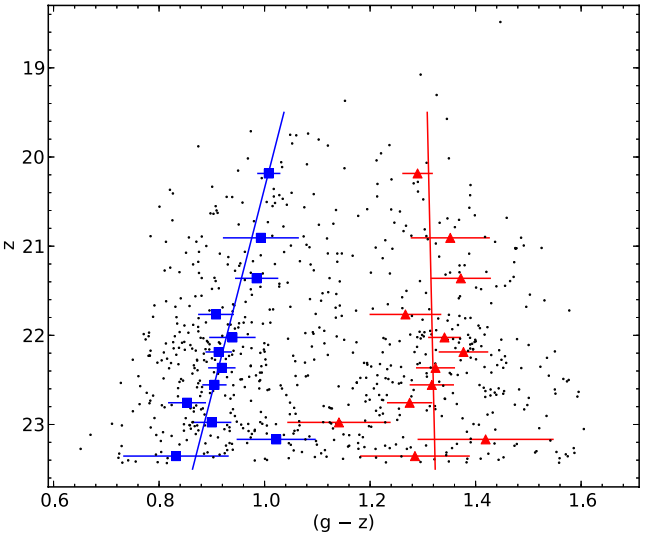

Figure 10. Colour–magnitude diagram of ACS GC candidates. The bimodal peaks found by GMM for each magnitude bin are overplotted with error bars in blue and red. The blue and red lines are the weighted least-squares fit to the blue and red peaks as a function of magnitude. NGC 4278 shows a significant blue tilt but does not show any evidence for a red tilt. Fainter than $z = 21.58$ ($M_z = -9.39$), there is no evidence of a colour–magnitude relation.

lack of a blue tilt at fainter magnitudes. Since the red GCs form with a much higher metallicity they experience a much smaller fractional change in metallicity due to self-enrichment and would be expected to show a much weaker colour–magnitude relation compared to the blue subpopulation.

To quantify any colour–magnitude relation, we split the ACS GC candidates by z-band magnitude into 12 bins of equal size. In each bin, we used GMM to find the peaks of the red and blue subpopulations. We then fit colour as a function of z-band magnitude using the mean magnitude of the GC candidates in each bin. The peaks found by GMM along with the fitted colour–magnitude relations are plotted on the colour–magnitude diagram in Fig. 10. The blue subpopulation shows a clear blue tilt:

$$(g-z)_{\rm blue} = (-0.043 \pm 0.008)M_z + (1.015 \pm 0.018), \quad (5)$$

while the red subpopulation does not show evidence for a colour–magnitude relation:

$$(g-z)_{\rm red} = (-0.004 \pm 0.014)M_z + (1.310 \pm 0.028). \quad (6)$$

These results are insensitive to the bin size used. The χ^2 value of the blue fit (7.0, 10 degrees of freedom) is significantly less than the χ^2 value for a constant colour (25.0, 11 degrees of freedom). The red fit and a constant colour for the red subpopulation both have χ^2 values of 9.6 and 9.7, respectively (10 and 11 degrees of freedom, respectively). We repeated the fits using only the nine faintest bins which corresponds to fitting all candidates fainter than $z = 21.58$ (or less massive than $5.8 \times 10^5\,{\rm M}_\odot$ using a mean mass-to-light ratio $\Upsilon_z = 1.9$ calculated from the stellar population models of Conroy et al. 2009 for an age of 12.6 Gyr, a Kroupa initial mass function and the observed GC colour distribution) and found no evidence for a colour–magnitude relation in either subpopulation (blue slope -0.018 ± 0.027 mag mag^{-1}, red slope -0.051 ± 0.043 mag mag^{-1}). We also repeated the fits using only the brightest six bins which corresponds to fitting all candidates brighter than $z = 22.27$ (or more massive than $3.1 \times 10^5\,{\rm M}_\odot$) finding a blue slope ($-0.048 \pm 0.009$ mag mag^{-1}) and a red slope (0.029 ± 0.015 mag mag^{-1}) slightly steeper but consistent with the slopes from the fits to all candidates. Additionally, we spilt the candidates into two equally sized bins by galactocentric radius. In the inner bin, with a mean galactocentric radius of 4.0 kpc, we found a blue slope of -0.068 ± 0.021 mag mag^{-1} and a red slope of 0.004 ± 0.025 mag mag^{-1}. In the outer bin, with a mean galactocentric radius of 11.2 kpc, we found a blue slope of -0.006 ± 0.026 mag mag^{-1} and a red slope of 0.010 ± 0.032 mag mag^{-1}.

The slopes of the colour–magnitude relations for both GC subpopulations are consistent with those observed by Mieske et al. (2010). Using the colour–metallicity relation of U12 and by assuming a constant mass-to-light ratio within each subpopulation, the slopes correspond to metallicity–mass slopes of $Z \propto M^{0.28 \pm 0.06}$ and $Z \propto M^{0.01 \pm 0.12}$ for the blue and red subpopulations, respectively. Using the colour–metallicity relation of Peng et al. (2006), the mass–metallicity relations are $Z \propto M^{0.55 \pm 0.10}$ and $Z \propto M^{0.02 \pm 0.06}$. The lack of a colour–magnitude relation at magnitudes fainter than ($M_z = -9.39$) is in line with the observations of Harris (2009a) and Mieske et al. (2010) who both saw significantly weaker blue tilts for GCs fainter than $M_z \sim -9.5$. This suggests a mass threshold for the self-enrichment that causes the blue tilt. Like in other galaxies, the blue tilt in NGC 4278 is much stronger closer to the centre of the galaxy than further away (Mieske et al. 2006, 2010; Blom et al. 2012). That the blue tilt is weaker both in lower mass galaxies and in the outer parts of higher mass galaxies suggests the environment in which the GC forms affect the amount of self-enrichment that occurs.

4.2 Colour gradients

Although GC systems usually show global radial colour gradients (since the blue subpopulations are usually more spatially extended than the red subpopulation) radial colour gradients within both or one of the subpopulations have been seen in several galaxies including NGC 4472 (Geisler, Lee & Kim 1996), NGC 1399 (Forte et al. 2001; Bassino et al. 2006), NGC 4486 (Harris 2009b; Strader et al. 2011; Forte, Vega & Faifer 2012), NGC 1407 (Forbes et al. 2011), NGC 3923 (Faifer et al. 2011), NGC 3115 (Arnold et al. 2011; Faifer et al. 2011) and the six massive ellipticals in the study of Harris (2009a), as well in a large sample of early-type galaxies in the Virgo and Fornax clusters (Liu et al. 2011). Some galaxies such as NGC 4486 (Strader et al. 2011) and NGC 4649 (Strader et al. 2012) show a clear negative gradient in the blue subpopulation while showing evidence of substructure in the red subpopulation. Since GC colour traces metallicity (e.g. Brodie et al. 2012), these colour gradients represent metallicity gradients. Metallicity gradients have been seen within the GC subpopulations in the Milky Way (Zinn 1985; Harris 2001, 2009a) and in the metal poor subpopulation of M31 (Fan et al. 2008). In a handful of galaxies, including NGC 1407 (Forbes et al. 2011), NGC 4486 (Harris 2009b; Strader et al. 2011) and the Milky Way (Harris 2001), the colour or metallicity gradients flatten at large radii. This was interpreted by Forbes et al. (2011) as evidence for a two-phase galaxy assembly (e.g. Oser et al. 2010) where the centre of the galaxy was built up early by dissipative collapse and the galaxy halo later by minor mergers.

To look for radial colour gradients within each subpopulation, we split the ACS GC candidates brighter than the turnover magnitude into seven equally sized bins in radius. Within each bin we used GMM to find the peaks of the red and blue subpopulations. In each bin, GMM found strong evidence for bimodality. We then fit colour

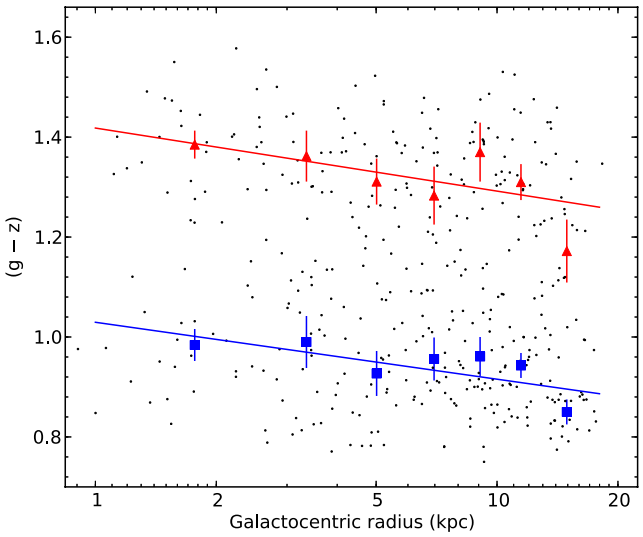

Figure 11. Colour versus galactocentric radius for ACS GC candidates brighter than the turnover magnitude. The bimodal peaks found by GMM for each radius bin are overplotted with error bars in blue and red. The curved blue and red lines are the linear-weighted least-squares fit to the blue and red peaks as a function of the logarithm of radius. The GC subpopulations in NGC 4278 show significant radial colour gradients.

as a function of the logarithm of the galactocentric radius using the mean galactocentric radius of the GC candidates in each bin. The peaks found by GMM along with the fitted colour–radius relations are plotted in Fig. 11. We found colour gradients within both the blue subpopulation:

$$(g-z)_{\rm blue} = (-0.114 \pm 0.047)\log R + (1.029 \pm 0.044) \quad (7)$$

and the red subpopulation:

$$(g-z)_{\rm red} = (-0.126 \pm 0.047)\log R + (1.418 \pm 0.035). \quad (8)$$

These results are independent of the number of bins used. The χ^2 values of the fits are lower than the χ^2 values for constant colour with radius for both the blue (7.2 versus 15.7, 5 and 6 degrees of freedom. respectively) and red (4.9 versus 12.2, 5 and 6 degrees of freedom, respectively) subpopulations. The $(g-z)$ gradients of the two subpopulations are consistent with one another.

We also used Gaussian kernel density estimation to examine the relationship between colour and radius as plotted in Fig. 12. We see similar results to those from GMM as the blue and red peaks move blueward with increasing radius. Using the peaks of the Gaussian kernel density estimates, we found colour gradients of -0.115 ± 0.025 and -0.126 ± 0.059 mag dex^{-1} for the blue and red subpopulations, respectively, consistent with the values obtained using GMM. Strader et al. (2012) noted that in NGC 4649, GCs brighter than the turnover showed different colour gradients than those in the magnitude range $21 < z < 23$ due to variations in the blue tilt with radius. Since the strength of the blue tilt varies with radius within NGC 4278 (Section 4.1), we measured the colour gradients of ACS candidates with magnitudes in the range $21 < z < 23$ and found gradients consistent with the colour gradients of GC candidates brighter than the turnover magnitude.

We also looked for colour gradients within the Suprime-Cam data set. As with the ACS data, we split Suprime-Cam candidates brighter than the turnover magnitude into nine equally sized bins by radius. Within each bin, we used GMM to find the peaks of the red and blue subpopulations. The peaks found by GMM along with the fitted

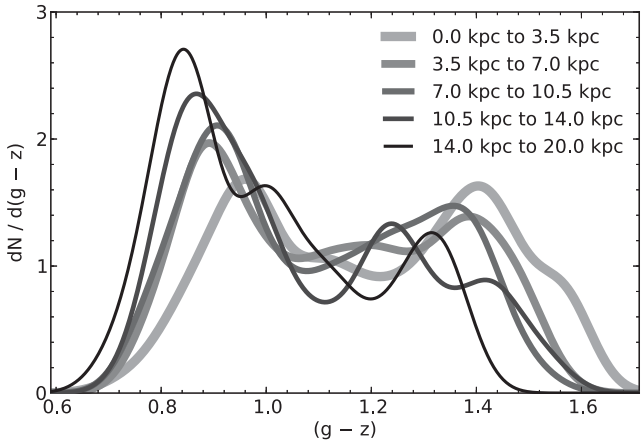

Figure 12. Gaussian kernel density estimation of the ACS colour distribution in radial bins. We used 3.5 kpc wide bins and a kernel size of $(g-z) = 0.05$. Lighter grey and wider lines corresponds to further from the galaxy. As in Fig. 11 the GC subpopulations shift to the blue with increasing radius.

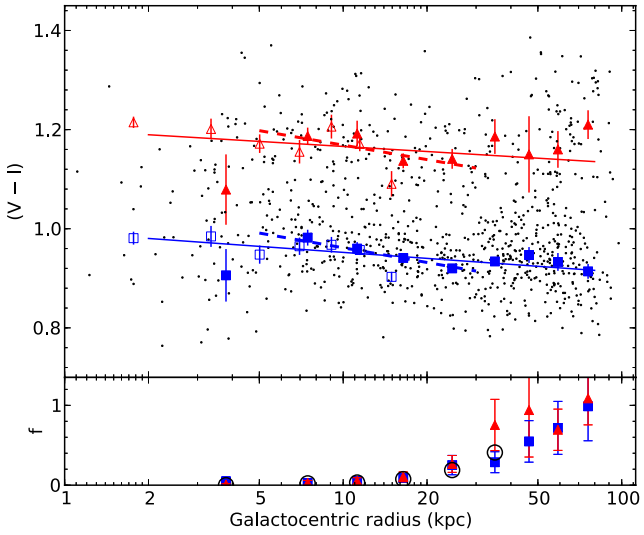

Figure 13. Suprime-Cam GC colour gradients. Top: colour versus galactocentric radius for Suprime-Cam GC candidates brighter than the turnover magnitude. The bimodal peaks found by GMM for each magnitude bin are plotted with error bars as solid blue squares and red triangles. The curved blue and red lines are the linear-weighted least-squares fit to the blue and red peaks as a function of the logarithm of radius. The dashed lines shows the fits to candidates between 5 and 30 pc. The open points show the GMM results for the ACS candidates. The GCs in NGC 4278 show significant radial colour gradients. The overdensity of red candidates at 80 kpc is not spatially collocated. Bottom: estimated contamination fraction for the two subpopulations in Suprime-Cam imaging. In each radial bin, the number of background objects predicted from the fitted background surface density and the bin's area are divided by the number of GCs GMM determines in each subpopulation. At 40 kpc more than 50 per cent of the candidates are likely background objects. The black open circles are the ratio of spectroscopic contaminants to all spectroscopically observed candidates in each bin. The number of spectroscopically observed candidates agrees with the number predicted from the surface density fitting.

colour–radius relations are plotted on the colour–radius diagram in the top part of Fig. 13. GMM did not favour a two-Gaussian fit over a one-Gaussian fit in the innermost bin; in the sixth and seventh bins the kurtosis was positive. We fit colour as a function of the logarithm

of the galactocentric radius using the mean galactocentric radius of the GC candidates in each bin. We found colour gradients within both the blue subpopulation:

$$(V-I)_{\rm blue} = (-0.040 \pm 0.018)\log R + (0.992 \pm 0.026) \quad (9)$$

and the red subpopulation:

$$(V-I)_{\rm red} = (-0.034 \pm 0.038)\log R + (1.225 \pm 0.040). \quad (10)$$

The outermost point was not included in the red fit. Within the radial range covered by the ACS imaging, we see agreement between the Suprime-Cam and ACS gradients. At large radii, where the Suprime-Cam data are most useful, contamination by foreground stars and background galaxies becomes an important consideration. Although we do not expect the colour of the contaminants to vary with radius, the contaminants could mask any colour gradient. We used the background surface densities from Section 3.1 to estimate what fraction of GCs are contaminants in each subpopulation at different radii. We plot the fraction in the lower part of Fig. 13. At 40 kpc more than half of the candidates are likely contaminants. We used the ratio of spectroscopically confirmed contaminants to all spectroscopically observed candidates in each bin to check the contaminant densities. The number of spectroscopic contaminants in each bin is consistent with the predicted level of contamination.

We repeated the fits for only candidates between 5 and 30 kpc of the galaxy split into five radial bins. We found slopes of -0.099 ± 0.015 and -0.097 ± 0.025 mag dex^{-1} for the blue and the red subpopulations, respectively. Converted into $(g-z)$, these slopes are steeper but consistent than those measured from the ACS data set and predict much redder colours within 5 pc than is observed from the ACS data set.

We see clear evidence for radial colour gradients in both GC subpopulations in the inner regions. Using the colour–metallicity relation of U12 we found that the ACS colour gradients correspond to metallicity gradients of -0.29 ± 0.12 and -0.32 ± 0.12 mag dex^{-1} for the blue and red subpopulation, respectively. Using the colour–metallicity relation of Peng et al. (2006), these correspond to -0.59 ± 0.24 and -0.23 ± 0.09 mag dex^{-1}. Unfortunately, the increasing level of contamination at larger radii makes it unclear whether we are observing a flat colour gradient in the outer regions or just the effects of a constant background in the Suprime-Cam data. We also note that a constant gradient in log radius appears to flatten at large radii in linear radius. While the red colour gradient is less clear than that of the blue, unlike in NGC 4649 (Strader et al. 2012) and in NGC 4486 (Strader et al. 2011), we do not see clear evidence for substructure in the red subpopulation. Low number statistics likely limit our ability to detect substructure.

The strengths of NGC 4278's GC colour gradients are steeper than the mean gradients observed in Virgo and Fornax early-type galaxies by Liu et al. (2011) but consistent with the observed scatter. Likewise NGC 4278's gradients are steeper than those observed in six early-type galaxies by Harris (2009a). However, NGC 4278's gradients are consistent with those of studies such as Forbes et al. (2011, NGC 1407), Arnold et al. (2011, NGC 3115), Blom et al. (2012, NGC 4365) and Strader et al. (2012, NGC 4649). For NGC 4278 and these studies, the strengths of the blue and red subpopulation gradients are consistent with one another. The connection between GC colour gradients and their host galaxies' properties will be discussed in depth in future SLUGGS survey papers.

5 GC SIZES

Previous observations (e.g. Kundu & Whitmore 2001; Larsen et al. 2001; Jordán et al. 2005; Masters et al. 2010) have shown that the sizes of GCs are consistent between galaxies of similar luminosities so much so that GC sizes have been suggested as a distance indicator (Kundu & Whitmore 2001). The mean size of the GCs of a galaxy varies weakly with galaxy luminosity; luminous galaxies have slightly smaller GCs than faint galaxies (Jordán et al. 2005; Georgiev et al. 2009; Masters et al. 2010). Remarkably, GC sizes are constant across more than two orders of magnitude of GC luminosity (e.g. McLaughlin 2000; Jordán et al. 2005). Only the brightest GCs show any size dependence on luminosity (e.g. Harris 2009a).

Although GC half-light radii are independent of magnitude (Jordán et al. 2005) for all but the brightest GCs (Harris 2009a), the sizes of GCs in the Milky Way have long been known to increase with distance from the Galactic Centre (van den Bergh 1956). Similar radial trends are seen in other galaxies (e.g. van den Bergh, Morbey & Pazder 1991; Spitler et al. 2006; Gómez & Woodley 2007; Harris 2009a; Blom et al. 2012). Since tidal fields that influence GC sizes and tidal fields are stronger closer to the centre of a galaxy, they provide a natural explanation for why GCs are smaller closer to the centres of galaxies (e.g. Madrid, Hurley & Sippel 2012). This could also explain why dwarf galaxies have larger GCs due to the weaker tidal forces in less massive galaxies. Alternatively, the larger sizes at larger radii could be an effect of the initial sizes being larger, as GC formation is still poorly understood.

Kundu & Whitmore (1998) first noticed that red GCs in NGC 3115 were ∼20 per cent smaller than blue ones. Similar differences in the half-light radii between the colour subpopulations have been seen in several studies including Larsen et al. (2001), Jordán et al. (2005), Harris (2009a) and Masters et al. (2010). Since the red subpopulation is in general more centrally concentrated (see Section 3.1) than the blue, and GC sizes increase with galactocentric radius, Larsen & Brodie (2003) argued that projection effects cause the apparent size difference between the subpopulations. However, Jordán (2004) proposed that mass segregation and the effects of metallicity on stellar evolution can produce the difference in half-light radius. Additionally, the initial sizes of GCs could be metallicity dependent.

Using the sizes calculated in Section 2.1, we find that the ACS GC candidates have a mean half-light radius of 2.64 ± 0.05 pc. This value agrees with previous work at our adopted distance and host galaxy luminosity (Jordán et al. 2005; Masters et al. 2010). Splitting the sample in two by colour, we found that the red GC candidates have a smaller mean half-light radius of 2.31 ± 0.07 pc and the blue GC candidates have a larger mean half-light radius of 2.99 ± 0.07 pc.

Using the ACS GC candidates, we explored the dependence of GC size on colour, galactocentric radius and luminosity. The relationships of colour, radius and luminosity with size are plotted in Fig. 14. We fitted a linear relation between the logarithm of the half-light radius and the colour:

$$\log r_{\rm hl} = \left(-0.316^{+0.035}_{-0.033}\right) \times (g-z) + \left(0.724^{+0.037}_{-0.039}\right). \quad (11)$$

The uncertainties in the fit were calculated using bootstrapping and the rms is 0.191 dex. We also split the candidates into two equal-sized bins by galactocentric radius and fitted the relationship between the logarithm of the half-light radius and the colour for each bin, finding the slopes in each bin to be smaller but consistent with that of the entire population.

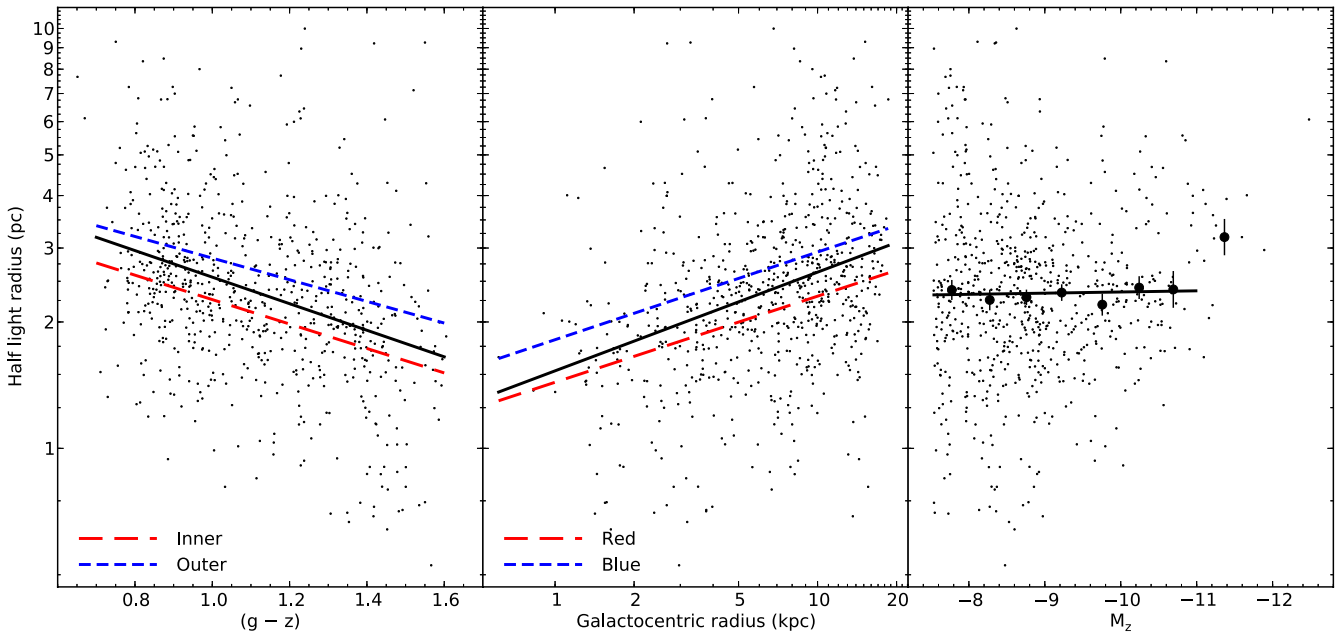

Figure 14. GC candidate sizes from ACS. Left: GC candidate half-light radius versus colour. The black line is the linear fit of the logarithm of the radius as a function of the colour. The short dashed blue line is the outer half of the candidates while the long dashed red line is the inner half of the candidates. Blue (metal poor) GCs are larger than red (metal rich) GCs, independent of galactocentric radius. Middle: half-light radius versus galactocentric radius. The black line is the power-law fit of half-light radius as a function of galactocentric radius. The short dashed blue line and the long dashed red line are the same fit for the blue and red subpopulations, respectively. Both blue and red GCs are larger further from the centre of the galaxy. Right: half-light radius versus absolute magnitude. The black circles are the median half-light radius in 0.5 mag bins; the brightest bin is all GCs brighter than $M_z = -11$. The black line is the linear fit of the logarithm of the radius as a function of magnitude restricted to GC candidates fainter than $M_z = -11$. The brightest GCs show a higher mean size than the bulk of the GC population.

We fitted a linear relation between the logarithm of the half-light radius and the logarithm of the galactocentric radius:

$$\log r_{\rm hl} = \left(0.235^{+0.023}_{-0.023}\right) \log R + \left(0.185^{+0.020}_{-0.021}\right). \quad (12)$$

The uncertainties in the fit were calculated using bootstrapping. We also fitted the relationship for the red and blue subpopulations separately, finding the slopes of the relations to be smaller but consistent with that of the entire population. Since colour changes with radius we fitted size as a function of both colour and radius simultaneously:

$$\log r_{\rm hl} = \left(0.193^{+0.023}_{-0.022}\right) \times \log R + \left(-0.263^{+0.031}_{-0.033}\right) \times (g - z) + \left(0.511^{+0.040}_{-0.041}\right). \quad (13)$$

The rms of this relation is 0.183 dex. Since we believe that the size measurement errors are reasonable (from the differences in the sizes measured for GCs appearing in multiple pointings) and much lower than this scatter (the mean error in log radius is 0.036 dex), this indicates that there is a large scatter in GC size at fixed colour and projected galactocentric radius.

In the right-hand panel of Fig. 14, we plot the median half-light radius in magnitude bins. The size of GCs appears to be constant with magnitude, apart from the brightest GCs. We fitted a linear relationship between the logarithm of the half-light radius and the z-band absolute magnitude for candidates fainter than $M_z = -11$, finding no significant relation:

$$\log r_{\rm hl} = (0.007^{+0.022}_{-0.025}) M_z + (0.472^{+0.195}_{-0.217}). \quad (14)$$

The uncertainties in the fit were calculated using bootstrapping and the relation has an rms of 0.204 dex. A Spearman's rank correlation test gives a correlation value of $\rho = -0.0059$ which corresponds to a probability of $p = 0.88$ that an uncorrelated population of the same size would produce the observed correlation value. A KS test shows a probability of 5.4×10^{-4} that GCs brighter than $M_z = -11$ are drawn from same distribution as the fainter GC candidates.

In Fig. 15, we plot the mean half-light radii of the blue and red GCs in radial bins. The ratio of the blue sizes to red sizes is independent of radius and has a mean value 1.21 ± 0.03. Using the median size rather than the mean size gave identical results as did using the mean of the log size. That the ratio is independent of galactocentric radius indicates that the apparent size difference between metal-poor and metal-rich GCs is caused by the effects of metallicity, not projection effects. Recent multipointing *HST* studies, such as those of NGC 4365 (Blom et al. 2012) and NGC 4649 (Strader et al. 2012), have similarly seen size differences at all radii. In the case of NGC 4649 (Strader et al. 2012), the size differences are observed at all radii despite the size being constant or decreasing beyond 15 kpc. Webb, Harris & Sills (2012b) simulated the effects of projection on their observations of GCs in NGC 4486. They concluded that projection effects cannot explain the observed size difference. Theoretical studies of GC dynamical evolution which include the effects of stellar evolution have produced an ∼20 per cent difference in half-light radius between metal-poor and metal-rich GC using both Monte Carlo techniques (Downing 2012) and direct N-body models (Sippel et al. 2012). The difference in half-light radius thus could be explained as a combination of mass segregation and the differences in stellar evolution of stars of different metallicities.

We observe a GC size–galactocentric radius relationship of $r_{\rm hl} \propto R^{0.19 \pm 0.02}$ after taking the effects of colour into account. Previous studies have revealed a range of power-law indices (α) for this relation with the Milky Way showing $\alpha = 0.46 \pm 0.05$ (Webb, Sills & Harris 2012a), the six giant galaxies studied by (Harris

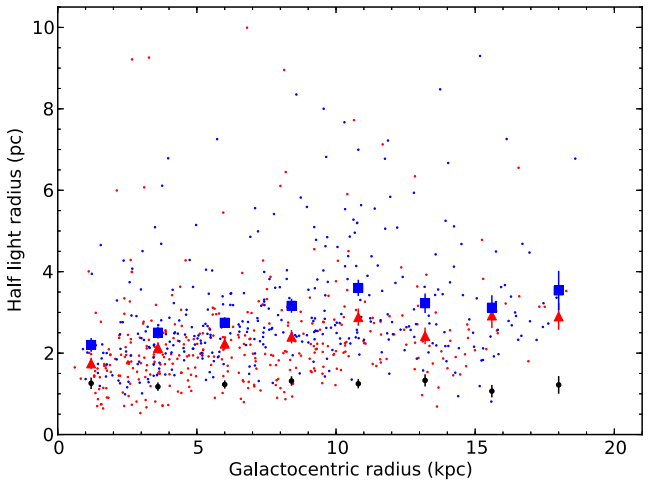

Figure 15. Half-light radius versus galactocentric radius for ACS GC candidates. Points are colour coded based on whether they are members of the blue or red subpopulations. The blue squares and red triangles are the mean half-light radii of the blue and red GCs, respectively, in 2.4 kpc wide bins. The black points are the ratio of the mean blue half-light radii to the mean red half-light radii. The ratio is constant with galactocentric radius suggesting that the difference in GC size between the two subpopulations is independent of galactocentric radius. Both subpopulations show a clear trend of increasing size with radius within 12 kpc ($5R_e$); beyond this radius the trend flattens.

2009a) showing $\alpha = 0.11$, NGC 4594 (Harris et al. 2010) showing $\alpha = 0.17 \pm 0.02$ and NGC 4365 (Blom et al. 2012) showing $\alpha = 0.47 \pm 0.02$. In both NGC 4649 (Strader et al. 2012) and NGC 1399 (Paolillo et al. 2011), only the inner (<15 kpc) GCs show a size–radius relation. In NGC 4278, the relationship between size and radius appears to be stronger within 12 kpc ($5R_e$) than beyond. This is consistent with the models of Madrid et al. (2012) where the relationship between size and radius flattens at large galactocentric radii. Since the tidal history of a GC affects its size, the sizes of GCs in a galaxy are dependent on its assembly history. Detailed models of GC sizes, spatial distributions and kinematics could be compared with observations to place constraints on the assembly history of a galaxy. We note that the tidal history, not just the tidal forces at the GC's current location, affect a GC's size. This at least partially explains the scatter in GC sizes observed even when accounting for galactocentric distance and colour. Additionally, projection effects likely cause some scatter as tidal forces are dependent on the true three-dimensional galactocentric radius, not on the observed projected radius.

In line with other galaxies (e.g. Harris 2009a), we found that GC size is independent of luminosity below $M_z \sim -11$ while brighter GCs have larger mean sizes. In common with massive early-type galaxies like NGC 4486 (Brodie et al. 2011) and NGC 4649 (Strader et al. 2012), NGC 4278 has a handful of UCD and UCD candidates (see Table 4). One UCD (acs_0320) is similar in half-light radius (23 pc), colour ($V - I = 0.92$) and absolute magnitude ($M_V = -9.6$) to the peculiar Milky Way GC NGC 2419 (Ibata et al. 2011; Cohen & Kirby 2012). The confirmed UCDs in NGC 4278 are discussed in more detail in Forbes et al. (2013).

6 SUMMARY

We used five *HST* ACS pointings and Subaru Suprime-Cam wide field imaging to study the GC system of NGC 4278. We used colours and sizes to select GC candidates from the ACS imaging and a colour–colour selection to identify GC candidates in the Suprime-Cam imaging. We also identified a handful of UCD candidates in the ACS imaging. Using new spectroscopy, we confirm two of the UCD candidates, and when combined with P13, bring the total number of spectroscopically confirmed GCs and UCDs in NGC 4278 to 270.

We measured the surface density profile of NGC 4278 GC candidates, finding that as in other galaxies, NGC 4278's blue GCs are more spatially extended than the red GCs. By integrating the surface density profile, we estimated the total number of GCs to be 1378^{+32}_{-194}. This corresponds to a specific frequency of $6.0^{+1.2}_{-1.3}$, making the GC system of NGC 4278 rich for its luminosity. Using the GC surface density profile, we were able to show that the nearby galaxy NGC 4283 makes an insignificant contribution to the NGC 4278 GC system and that NGC 4283 likely has a low number of GCs for its luminosity. Although NGC 4278's and NGC 4283's GC systems are rich and poor, respectively, for their luminosities, they are both within the observed scatter of the large sample of Harris et al. (2013).

Like almost all large galaxies, NGC 4278's GC system shows colour bimodality. A clear blue tilt is observed along with evidence that the blue tilt is stronger in the inner regions of the galaxy than in the outer regions. We observe clear radial colour gradients in both GC subpopulations. The gradients are present in both the ACS and Suprime-Cam data. Unfortunately, due to the level of contamination in the Suprime-Cam data, we could not reliably use them to probe the metallicity gradient much further than the coverage of the ACS data. This means that we cannot see if the gradients flatten at large radii as is the case in NGC 1407. When compared to colour gradients in other galaxies, NGC 4278's gradients are typical.

We also studied the relationships between GCs' half-light radii and their colours and positions within NGC 4278. We found that like other galaxies, GC sizes decrease with redder colours and increase with distance from NGC 4278. For GCs fainter than $M_z = -11$, we found no relationship between size and GC luminosity; GCs brighter than $M_z = -11$ have larger sizes than the fainter GCs. We found that the ratio of the sizes of blue GCs to red GCs is independent of galactocentric distance indicating that the apparent size difference between red and blue GCs is due to dynamical and stellar evolution and not to projection effects. Although NGC 4278 is a less luminous galaxy than previous multipointing studies of GC systems (e.g. NGC 4594, NGC 4365 and NGC 4649), the properties of NGC 4278's GC system are similar.

ACKNOWLEDGEMENTS

We wish to thank the referee for his useful comments which greatly improved the manuscript. We thank Vincenzo Pota and Christina Blom for their careful reading of the manuscript. We also thank Caroline Foster, Samantha Penny, Jacob Arnold, Christina Blom, Vincenzo Pota, Sreeja Kartha, Nicola Pastorello, Anna Sippel, Juan Madrid and Gonzalo Díaz for useful discussions. We acknowledge the usage of the HyperLeda data base (http://leda.univ-lyon1.fr). This publication makes use of data products from the Two Micron All Sky Survey, which is a joint project of the University of Massachusetts and the Infrared Processing and Analysis Center/California Institute of Technology, funded by the National Aeronautics and Space Administration and the National Science Foundation. This research has made use of the NASA/IPAC Extragalactic Database (NED) which is operated by the Jet Propulsion Laboratory, California Institute of Technology, under contract with the National Aeronautics and Space Administration. The analysis pipeline used to reduce the DEIMOS data was developed at UC Berkeley with

support from NSF grant AST-0071048. This publication made use of PYRAF and PYFITS which are products of the Space Telescope Science Institute, which is operated by AURA for NASA. This research made use of TOPCAT (Taylor 2005). Some of the data presented herein were obtained at the W. M. Keck Observatory, operated as a scientific partnership among the California Institute of Technology, the University of California and the National Aeronautics and Space Administration, and made possible by the generous financial support of the W. M. Keck Foundation. The authors wish to recognize and acknowledge the very significant cultural role and reverence that the summit of Mauna Kea has always had within the indigenous Hawaiian community. We are most fortunate to have the opportunity to conduct observations from this mountain. This research is based in part on data collected at Subaru Telescope, which is operated by the National Astronomical Observatory of Japan. This research is based on observations made with the NASA/ESA *Hubble Space Telescope*, obtained from the data archive at the Space Telescope Science Institute. STScI is operated by the Association of Universities for Research in Astronomy, Inc. under NASA contract NAS 5-26555. This work is also based upon work supported by the Australian Research Council under grant DP130100388 and by the National Science Foundation under grants AST-0909237, AST-1109878 and AST-1211995.

REFERENCES

Abazajian K. N. et al., 2009, ApJS, 182, 543
Alves-Brito A., Hau G. K. T., Forbes D. A., Spitler L. R., Strader J., Brodie J. P., Rhode K. L., 2011, MNRAS, 417, 1823
Arnold J. A., Romanowsky A. J., Brodie J. P., Chomiuk L., Spitler L. R., Strader J., Benson A. J., Forbes D. A., 2011, ApJ, 736, L26
Baba H. et al., 2002, in Bohlender D. A., Durand D., Handley T. H., eds, ASP Conf. Ser. Vol. 281, Astronomical Data Analysis Software and Systems XI, Astron. Soc. Pac., San Francisco, p. 298
Bailin J., Harris W. E., 2009, ApJ, 695, 1082
Bassino L. P., Faifer F. R., Forte J. C., Dirsch B., Richtler T., Geisler D., Schuberth Y., 2006, A&A, 451, 789
Beasley M. A., Bridges T., Peng E., Harris W. E., Harris G. L. H., Forbes D. A., Mackie G., 2008, MNRAS, 386, 1443
Blakeslee J. P., Lucey J. R., Barris B. J., Hudson M. J., Tonry J. L., 2001, MNRAS, 327, 1004
Blom C., Spitler L. R., Forbes D. A., 2012, MNRAS, 420, 37
Brassington N. J. et al., 2009, ApJS, 181, 605
Brodie J. P., Strader J., 2006, ARA&A, 44, 193
Brodie J. P., Romanowsky A. J., Strader J., Forbes D. A., 2011, AJ, 142, 199
Brodie J. P., Usher C., Conroy C., Strader J., Arnold J. A., Forbes D. A., Romanowsky A. J., 2012, ApJ, 759, L33
Burkert A., Tremaine S., 2010, ApJ, 720, 516
Cappellari M. et al., 2011, MNRAS, 413, 813
Cappellari M. et al., 2013, MNRAS, 432, 1709
Chies-Santos A. L., Larsen S. S., Wehner E. M., Kuntschner H., Strader J., Brodie J. P., 2011a, A&A, 525, A19
Chies-Santos A. L., Larsen S. S., Kuntschner H., Anders P., Wehner E. M., Strader J., Brodie J. P., Santos J. F. C., 2011b, A&A, 525, A20
Chies-Santos A. L., Larsen S. S., Cantiello M., Strader J., Kuntschner H., Wehner E. M., Brodie J. P., 2012, A&A, 539, A54
Ciardullo R., 2012, Ap&SS, 341, 151
Ciardullo R., Feldmeier J. J., Jacoby G. H., Kuzio de Naray R., Laychak M. B., Durrell P. R., 2002, ApJ, 577, 31
Cohen J. G., Kirby E. N., 2012, ApJ, 760, 86
Conroy C., Gunn J. E., White M., 2009, ApJ, 699, 486
Cooper M. C., Newman J. A., Davis M., Finkbeiner D. P., Gerke B. F., 2012, in Astrophysics Source Code Library, record ascl:1203.003, p. 3003
Côté P. et al., 2004, ApJS, 153, 223
de Vaucouleurs G., de Vaucouleurs A., Corwin H. G., Jr, Buta R. J., Paturel G., Fouque P., 1991, in de Vaucouleurs G., de Vaucouleurs A., Corwin H. G., Jr, Buta R. J., Paturel G., Fouque P., eds, Third Reference Catalogue of Bright Galaxies. Springer-Verlag, Berlin
Downing J. M. B., 2012, MNRAS, 425, 2234
Fabbiano G. et al., 2010, ApJ, 725, 1824
Faifer F. R. et al., 2011, MNRAS, 416, 155
Fan Z., Ma J., de Grijs R., Zhou X., 2008, MNRAS, 385, 1973
Forbes D. A., 1996, AJ, 112, 1409
Forbes D. A., 2005, ApJ, 635, L137
Forbes D. A., Franx M., Illingworth G. D., Carollo C. M., 1996, ApJ, 467, 126
Forbes D. A., Beasley M. A., Brodie J. P., Kissler-Patig M., 2001, ApJ, 563, L143
Forbes D. A., Spitler L. R., Strader J., Romanowsky A. J., Brodie J. P., Foster C., 2011, MNRAS, 413, 2943
Forbes D. A., Ponman T., O'Sullivan E., 2012, MNRAS, 425, 66
Forbes D., Pota V., Usher C., Strader J., Romanowsky A., Brodie J., Arnold J., Spitler L., 2013, MNRAS, 435, L6
Forte J. C., Geisler D., Ostrov P. G., Piatti A. E., Gieren W., 2001, AJ, 121, 1992
Forte J. C., Vega E. I., Faifer F., 2012, MNRAS, 421, 635
Foster C., Forbes D. A., Proctor R. N., Strader J., Brodie J. P., Spitler L. R., 2010, AJ, 139, 1566
Geisler D., Lee M. G., Kim E., 1996, AJ, 111, 1529
Georgiev I. Y., Puzia T. H., Hilker M., Goudfrooij P., 2009, MNRAS, 392, 879
Georgiev I. Y., Puzia T. H., Goudfrooij P., Hilker M., 2010, MNRAS, 406, 1967
Giroletti M., Taylor G. B., Giovannini G., 2005, ApJ, 622, 178
Gómez M., Woodley K. A., 2007, ApJ, 670, L105
Graham A. W., Driver S. P., 2005, Publ. Astron. Soc. Aust., 22, 118
Gregory S. A., Thompson L. A., 1977, ApJ, 213, 345
Hargis J. R., Rhode K. L., 2012, AJ, 144, 164
Harris W. E., 2001, in Labhardt L., Binggeli B., eds, Saas-Fee Advanced Course 28: Star Clusters. Springer-Verlag, Berlin, p. 223
Harris W. E., 2009a, ApJ, 699, 254
Harris W. E., 2009b, ApJ, 703, 939
Harris G. L. H., Harris W. E., 2011, MNRAS, 410, 2347
Harris W. E., van den Bergh S., 1981, AJ, 86, 1627
Harris W. E., Spitler L. R., Forbes D. A., Bailin J., 2010, MNRAS, 401, 1965
Harris W. E., Whitmore B. C., Karakla D., Okoń W., Baum W. A., Hanes D. A., Kavelaars J. J., 2006, ApJ, 636, 90
Harris W. E., Harris G. L. H., Alessi M., 2013, ApJ, 772, 82
Ibata R., Sollima A., Nipoti C., Bellazzini M., Chapman S. C., Dalessandro E., 2011, ApJ, 738, 186
Ivezić Ž. et al., 2007, AJ, 134, 973
Jacoby G. H., Ciardullo R., Harris W. E., 1996, ApJ, 462, 1
Jordán A., 2004, ApJ, 613, L117
Jordán A. et al., 2005, ApJ, 634, 1002
Jordán A. et al., 2007, ApJS, 169, 213
King I., 1962, AJ, 67, 471
Kundu A., Whitmore B. C., 1998, AJ, 116, 2841
Kundu A., Whitmore B. C., 2001, AJ, 121, 2950
Kuntschner H. et al., 2010, MNRAS, 408, 97
Landolt A. U., 1992, AJ, 104, 340
Larsen S. S., 1999, A&AS, 139, 393
Larsen S. S., Brodie J. P., 2003, ApJ, 593, 340
Larsen S. S., Brodie J. P., Huchra J. P., Forbes D. A., Grillmair C. J., 2001, AJ, 121, 2974
Liu C., Peng E. W., Jordán A., Ferrarese L., Blakeslee J. P., Côté P., Mei S., 2011, ApJ, 728, 116
Madrid J. P., Hurley J. R., Sippel A. C., 2012, ApJ, 756, 167
Masters K. L. et al., 2010, ApJ, 715, 1419
McLaughlin D. E., 2000, ApJ, 539, 618
Mei S. et al., 2007, ApJ, 655, 144
Mieske S. et al., 2006, ApJ, 653, 193

Mieske S. et al., 2010, ApJ, 710, 1672
Miyazaki S. et al., 2002, PASJ, 54, 833
Monet D. G. et al., 2003, AJ, 125, 984
Morganti R. et al., 2006, MNRAS, 371, 157
Muratov A. L., Gnedin O. Y., 2010, ApJ, 718, 1266
Newman J. A. et al., 2013, ApJS, 208, 5
Oser L., Ostriker J. P., Naab T., Johansson P. H., Burkert A., 2010, ApJ, 725, 2312
Ouchi M. et al., 2004, ApJ, 611, 660
Paolillo M., Puzia T. H., Goudfrooij P., Zepf S. E., Maccarone T. J., Kundu A., Fabbiano G., Angelini L., 2011, ApJ, 736, 90
Park H. S., Lee M. G., 2013, ApJ, 773, L27
Peng E. W. et al., 2006, ApJ, 639, 95
Peng E. W. et al., 2008, ApJ, 681, 197
Pota V. et al., 2013, MNRAS, 428, 389 (P13)
Puzia T. H., Kissler-Patig M., Thomas D., Maraston C., Saglia R. P., Bender R., Goudfrooij P., Hempel M., 2005, A&A, 439, 997
Rhode K. L., 2012, AJ, 144, 154
Schlegel D. J., Finkbeiner D. P., Davis M., 1998, ApJ, 500, 525
Sérsic J. L., 1963, Boletin de la Asociacion Argentina de Astronomia La Plata Argentina, 6, 41
Shapiro K. L. et al., 2010, MNRAS, 402, 2140
Sippel A. C., Hurley J. R., Madrid J. P., Harris W. E., 2012, MNRAS, 427, 167
Sirianni M. et al., 2005, PASP, 117, 1049
Skrutskie M. F. et al., 2006, AJ, 131, 1163
Spitler L. R., Forbes D. A., 2009, MNRAS, 392, L1
Spitler L. R., Larsen S. S., Strader J., Brodie J. P., Forbes D. A., Beasley M. A., 2006, AJ, 132, 1593
Stetson P. B., 1992, in Worrall D. M., Biemesderfer C., Barnes J., eds, ASP Conf. Ser. Vol. 25, Astronomical Data Analysis Software and Systems I. Astron. Soc. Pac., San Francisco, p. 297
Stetson P. B., 2000, PASP, 112, 925
Strader J., Smith G. H., 2008, AJ, 136, 1828
Strader J., Brodie J. P., Cenarro A. J., Beasley M. A., Forbes D. A., 2005, AJ, 130, 1315
Strader J., Brodie J. P., Spitler L., Beasley M. A., 2006, AJ, 132, 2333
Strader J., Beasley M. A., Brodie J. P., 2007, AJ, 133, 2015
Strader J. et al., 2011, ApJS, 197, 33
Strader J. et al., 2012, ApJ, 760, 87
Taylor M. B., 2005, in Shopbell P., Britton M., Ebert R., eds, ASP Conf. Ser. Vol. 347, Astronomical Data Analysis Software and Systems XIV. Astron. Soc. Pac., San Francisco, p. 29
Tonry J. L., Dressler A., Blakeslee J. P., Ajhar E. A., Fletcher A. B., Luppino G. A., Metzger M. R., Moore C. B., 2001, ApJ, 546, 681
Tully R. B., Fisher J. R., 1988, Catalog of Nearby Galaxies. Cambridge Univ. Press, Cambridge
Usher C. et al., 2012, MNRAS, 426, 1475 (U12)
van den Bergh S., 1956, Z. Astrophys., 41, 61
van den Bergh S., Morbey C., Pazder J., 1991, ApJ, 375, 594
Vazdekis A., Cenarro A. J., Gorgas J., Cardiel N., Peletier R. F., 2003, MNRAS, 340, 1317
Villegas D. et al., 2010, ApJ, 717, 603
Webb J. J., Sills A., Harris W. E., 2012a, ApJ, 746, 93
Webb J. J., Harris W. E., Sills A., 2012b, ApJ, 759, L39
Yagi M. et al., 2002, in Starck J.-L., Murtagh F. D., eds, Proc. SPIE Conf. Ser. Vol. 4847, Astronomical Data Analysis II. SPIE, Bellingham, p. 322
Yoon S., Yi S. K., Lee Y., 2006, Sci, 311, 1129
Yoon S.-J. et al., 2011, ApJ, 743, 150
Younes G., Porquet D., Sabra B., Grosso N., Reeves J. N., Allen M. G., 2010, A&A, 517, A33
Zinn R., 1985, ApJ, 293, 424

APPENDIX A: SPECTROSCOPICALLY CONFIRMED OBJECTS

Table A1. Spectroscopically confirmed GCs, galaxies and stars.

Name	RA	Dec.	$(g-z)$	z	$r_{\rm hl}$	$(B-V)$	$(V-I)$	I	v	[Z/H]
	(°)	(°)	(mag)	(mag)	(pc)	(mag)	(mag)	(mag)	(km s^{-1})	(dex)
(1)	(2)	(3)	(4)	(5)	(6)	(7)	(8)	(9)	(10)	(11)
NGC 4278_GC1	185.079 334	29.258 192	0.91 ± 0.03	22.19 ± 0.02	3.4 ± 0.3	0.72 ± 0.05	1.06 ± 0.04	21.66 ± 0.03	307 ± 10	–
NGC 4278_GC2	185.018 457	29.295 004	0.84 ± 0.02	22.08 ± 0.01	2.0 ± 0.1	0.83 ± 0.06	0.91 ± 0.05	21.69 ± 0.04	668 ± 13	–
NGC 4278_GC3	185.038 466	29.276 498	0.81 ± 0.02	20.95 ± 0.01	2.9 ± 0.1	0.73 ± 0.04	0.90 ± 0.04	20.33 ± 0.04	1225 ± 8	$-1.93^{+0.32}_{-0.13}$
NGC 4278_GC4	185.001 351	29.315 286	0.95 ± 0.03	21.22 ± 0.01	5.6 ± 0.2	0.81 ± 0.04	0.99 ± 0.03	20.73 ± 0.02	394 ± 11	$-1.37^{+0.25}_{-0.22}$
NGC 4278_GC5	185.032 302	29.289 058	1.15 ± 0.01	20.13 ± 0.01	2.1 ± 0.0	0.95 ± 0.04	1.08 ± 0.03	19.86 ± 0.02	235 ± 8	$0.20^{+0.18}_{-0.43}$
...	...	...	...	...	...	...	...	...	...	...
NGC 4278_gal1	185.002 305	29.331 285	0.99 ± 0.16	24.66 ± 0.10	2.9 ± 1.7	–	–	–	$z = 0.74$	–
NGC 4278_gal2	185.061 485	29.242 873	1.16 ± 0.05	23.12 ± 0.03	1.9 ± 0.4	–	–	–	$z = 0.43$	–
NGC 4278_gal3	184.903 458	29.276 536	–	–	–	0.66 ± 0.04	0.86 ± 0.03	21.09 ± 0.02	$z = 0.20$	–
NGC 4278_gal4	185.084 196	29.296 686	0.83 ± 0.03	22.22 ± 0.02	5.3 ± 0.2	0.83 ± 0.05	0.78 ± 0.04	21.85 ± 0.03	$z = 0.44$	–
NGC 4278_gal5	185.139 871	29.253 525	–	–	–	0.73 ± 0.04	0.79 ± 0.03	21.75 ± 0.03	$z = 0.15$	–
...	...	...	...	...	...	...	...	...	...	...
NGC 4278_stars1	185.065 617	29.286 417	3.84 ± 0.05	21.27 ± 0.01	0.1 ± 0.1	0.33 ± 0.10	2.93 ± 0.08	21.28 ± 0.05	-42 ± 18	–
NGC 4278_stars2	185.027 350	29.252 617	0.98 ± 0.02	20.56 ± 0.01	0.0 ± 0.1	0.89 ± 0.04	0.99 ± 0.03	20.15 ± 0.02	92 ± 11	–
NGC 4278_stars3	185.006 250	29.264 183	2.77 ± 0.02	17.69 ± 0.01	0.0 ± 0.0	1.72 ± 0.06	2.15 ± 0.05	17.51 ± 0.04	-6 ± 5	–
NGC 4278_stars4	185.090 008	29.184 019	–	–	–	0.74 ± 0.03	0.92 ± 0.03	18.01 ± 0.02	117 ± 5	–
NGC 4278_stars5	185.074 267	29.188 356	–	–	–	1.01 ± 0.03	1.08 ± 0.03	17.01 ± 0.02	7 ± 6	–
...	...	...	...	...	...	...	...	...	...	...

Notes. Column (1): identifier from P13. GC designations start with NGC 4278_GC, galaxy designations with NGC 4278_gal and star designations with NGC 4278_stars. For objects that were observed spectroscopically for the first time in this work, we have extended the P13 naming scheme to them. Column (2) and (3): right ascension and declination in the J2000.0 epoch, respectively. Column (4): ACS $(g-z)$ colour. Column (5): ACS z-band magnitude. Column (6): half-light radius in parsecs if the object was at our adopted distance of 15.6 Mpc. Column (4): Suprime-Cam $(B-V)$ colour. Column (5): Suprime-Cam $(V-I)$ colour. Column (6): Suprime-Cam I-band magnitude. Column (7): radial velocity. For galaxies this is the estimated redshift. Column (8): calcium triplet metallicity. Column (9): identifier from P13. The full version of this table is provided in a machine readable form in the online Supporting Information.

SUPPORTING INFORMATION

Additional Supporting Information may be found in the online version of this article:

Table 3. ACS GC candidates.
Table 5. Suprime-Cam GC candidates.
Table A1. Spectroscopically confirmed GCs, galaxies and stars.
(http://mnras.oxfordjournals.org/lookup/suppl/doi:10.1093/mnras/stt1637/-/DC1)

Please note: Oxford University Press are not responsible for the content or functionality of any supporting materials supplied by the authors. Any queries (other than missing material) should be directed to the corresponding author for the paper.

This paper has been typeset from a TEX/LATEX file prepared by the author.